Engineering Structures 305 (2024) 117758

Contents lists available at ScienceDirect

Engineering Structures

journal homepage: www.elsevier.com/locate/engstruct

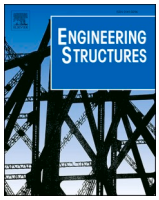

Lateral-torsional buckling resistance of non-prismatic and prismatic mono-symmetric I-section steel beams based on stress utilization

J.O. Gomes Jr. [a,b], L. Simões da Silva [a,*], T. Tankova [c], H. Carvalho [b,d], J.O. Ferreira Filho [a]

[a] University of Coimbra, ISISE, ARISE, Department of Civil Engineering, Coimbra, Portugal
[b] Federal University of Minas Gerais, Department of Structural Engineering, Belo Horizonte, Minas Gerais, Brazil
[c] Delft University of Technology, Department of Engineering Structures, Delft, Netherlands
[d] University of São Paulo, Department of Structural Engineering and Geotechnical, São Paulo, Brazil

ARTICLE INFO

Keywords:
Stability
Steel
Eurocode 3
General formulation
Mono-symmetric beams

ABSTRACT

The lateral-torsional resistance of prismatic double-symmetric I-section beams is accurately predicted using a mechanically consistent Ayrton-Perry approach, combined with a calibrated generalized imperfection. The corresponding design formulation was recently adopted in the revised version of Eurocode 3. However, for prismatic mono-symmetric I-section beams, the General Case shall be used while for non-prismatic beams only the General Method is available. Both methods present a very large scatter and highly underestimate the lateral-torsional buckling resistance. This paper proposes an extension to the General Formulation for non-prismatic beams with arbitrary boundary conditions, partial lateral restraints, and arbitrary loading for mono-symmetric I-sections. Using an advanced numerical model calibrated with experimental test results, a large parametric study is undertaken, and its results are used to assess the available design methodologies and the proposed method. It is concluded that the General Formulation provides excellent safe-sided estimates of the LTB resistance, and it is confirmed the very poor performance of the General Case and the General Method.

1. Introduction

Thin-walled welded steel mono-symmetric I-sections provide a cost-efficient solution due to their efficiency in bending and ease of fabrication [1]. When used in non-prismatic members, mono-symmetric sections allow to adjust the resistance of the section to a variable bending moment along the member, thereby potentially maximizing the efficiency of the design. Tapered steel beams with mono-symmetric I-sections are widely used in crane girders, pitched-roof portal frames and in twin or multiple girder bridge decks, often as part of composite girders.

The lateral-torsional buckling resistance of prismatic mono-symmetric steel beams is tackled in part 1–1 of Eurocode 3 [2], henceforth denoted to as EC3–1-1, using the General Case (GC), that is based on the analogy between N_{cr} and M_{cr} and the assumption that the lateral-torsional buckling behavior of a beam in bending is similar to a compressed column [3]. This contrasts with the new method for doubly symmetric I- and H-sections (newLTB) that is now included in FprEN 1993–1-1 [4], which is based on a mechanically consistent Ayrton-Perry derivation ([5,6]). It was shown [7] that the GC is too conservative and presents a large scatter of results, while the newLTB presents a good agreement with a large set of experimental and validated numerical results and a low scatter.

Concerning non-prismatic beams, EC3–1-1 proposes the General Method (GM), which is a Merchant-Rankine semi-empirical method that leads to a very wide scatter of results that may even be unsafe [7]. In the case of prismatic beams, it was demonstrated that the GM leads to the same results as the GC [7].

Recently, Tankova et al. [8] proposed a design-oriented method, General Formulation (GF) that can verify the buckling resistance of an arbitrary non-prismatic member, with arbitrary boundary conditions, variable loading and partial lateral restraints for double symmetric I- or H-sections. This paper presents an extension of the General Formulation [8] to generic non-prismatic mono-symmetric cross-section beams. Firstly, a brief state-of-the-art on mono-symmetric members and tapered members is presented, followed by the analytical derivation of the extended formulation that specifically accounts for the mono-symmetric features. Subsequently, an advanced finite element model is validated with experimental results on mono-symmetric beams and some benchmarks obtained from the literature, followed by an extensive parametric study for class 1 and class 2 cross-sections with prismatic and

* Correspondence to: Department of Civil Engineering, University of Coimbra, Polo II, Pinhal de Marrocos, 3030-290 Coimbra, Portugal.
E-mail address: luisss@dec.uc.pt (L. Simões da Silva).

https://doi.org/10.1016/j.engstruct.2024.117758
Received 8 September 2023; Received in revised form 17 December 2023; Accepted 25 February 2024
Available online 5 March 2024

Nomenclature

Lowercase Latin letters

b_1, b_2	Flange width
e_0	Maximum amplitude of a member imperfection
f_y	Yield stress
h	Cross section depth
n	Number of cases
r_0	Polar radius of gyration about the shear center
r_e	Ratio between the numerical lateral-torsional buckling resistance and the plastic bending moment resistance of the cross section
r_N	Ratio between the numerical lateral-torsional buckling resistance and the analytical lateral-torsional buckling resistance
r_t	Ratio between the analytical buckling resistance and the cross-sectional plastic bending moment resistance
t_1, t_2	Flange thickness
t_w	Web thickness
v(x)	Transverse displacement along the y-axis
v_0(x)	Initial transverse displacement along the y-axis
v_{cr}(x)	Transverse displacement component of the mode shape along the y-axis
v_{tot}(x)	Total transverse displacement [v(x) + v_0(x)] along the y-axis
x-x	Axis along the member
x_m	Critical location
y-y	Cross section axis parallel to the flanges
z-z	Cross section axis perpendicular to the flanges
z_G	Position of the cross-section centroid measured from the top face of the largest flange
z_0	Distance between the centroid and the torsion center of the cross section

Uppercase Latin letters

A	Cross section area
C_i	Equivalent moment factor
C_w	Warping constant
E	Modulus of elasticity
G	Shear Modulus
I_y	Moment of inertia about the y-axis
I_z	Moment of inertia about the z-axis
J	Torsional constant
L	Member length
M	Bending moment
M_{cr}	Elastic critical moment
M_{Ed}	Design bending moment
M_{pl}	Plastic bending moment resistance about the y-y axis
M_y	Bending moment, y-y axis
M_y^{II}	Second order bending moment, y-y axis
M_z	Bending moments, z-z axis
M_w^{II}	Second order warping moment
M_z^{II}	Second order bending moment, z-z axis
N	Normal force
N_{cr}	Elastic critical force
$N_{cr,TF}$	Elastic critical force for torsional-flexural buckling
$N_{cr,x}$	Elastic critical force for torsional buckling
$N_{cr,z}$	Elastic critical force for out-of-plane buckling
W_w	Elastic warping modulus
W_y	Section modulus about the y-y axis
$W_{y,el}$	Elastic section modulus about the y-y axis
W_z	Section modulus about the z-z axis
$W_{z,el}$	Elastic section modulus about the z-z axis

Lowercase Greek letters

α	Imperfection factor according to EC3–1-1
α_{cr}	Load multiplier which leads to the elastic critical resistance
$\alpha_{cr,op}$	Minimum amplifier for the in-plane design loads to reach the elastic critical resistance with regard to lateral or lateral-torsional buckling
α_{LT}	Imperfection factor for lateral-torsional buckling
$\alpha_{ult,k}$	Minimum load amplifier of the design loads to reach the characteristic resistance of the most critical cross section
β_z	Wagner factor
δ_0	General displacement of the imperfect shape
δ_{cr}	General displacement of the critical mode
ε_M	Utilization ratio regarding the bending moment
ε_M^I	Utilization ratio regarding the first-order bending moment
ε_M^{II}	Utilization ratio regarding the second-order bending moment
η	Generalized imperfection
$\overline{\lambda}_{op}$	Global non-dimensional slenderness of a structural component for out-of-plane buckling according to the General Method (of clause 6.3.4)
$\overline{\lambda}$	Non-dimensional slenderness
$\overline{\lambda}(x)$	Non-dimensional slenderness at a given position
$\overline{\lambda}_z$	Non-dimensional slenderness for flexural buckling, z-z axis
$\overline{\lambda}_{LT}$	Non-dimensional slenderness for lateral-torsional buckling
θ(x)	Twist rotation
θ_0(x)	Initial twist rotation
θ_{cr}(x)	Twist rotation component of the mode shape
θ_{tot}(x)	Total twist rotation [θ(x) + θ_0(x)]
χ	Reduction factor.
χ_{LT}	Reduction factor due to lateral-torsional buckling
χ_{op}	Reduction factor corresponding to the non-dimensional slenderness $\overline{\lambda}_{op}$
ψ	Ratio between the maximum and minimum bending moments, for a linear bending moment distribution

Uppercase Greek letters

Φ_{LT}	Value to determine the reduction factor χ_{LT} for lateral-torsional buckling

non-prismatic beams. Finally, the results are compared to the various available design methodologies and the proposed extended GF, showing the good performance of the method.

2. Literature review

2.1. Theoretical background

Fig. 1 shows a typical mono-symmetric I-section studied in this work. This section is symmetric with respect to the minor axis, z, and asymmetric around the major axis, y. The members are subjected to bending moment around y-axis. In this figure, b_1 and t_1 are the dimensions of the flange with the smallest value of I_z (moment of inertia about the z-axis), and b_2 and t_2 are the dimensions of the largest flange; G and D are the centroid and the torsion center, respectively.

According to Vlasov's Theory [9], for a uniform mono-symmetric I-sections subjected to constant bending moment around the major axis (M_y), the equilibrium of the deformed shape of a perfect (with no imperfections) member is ruled by the following equations:

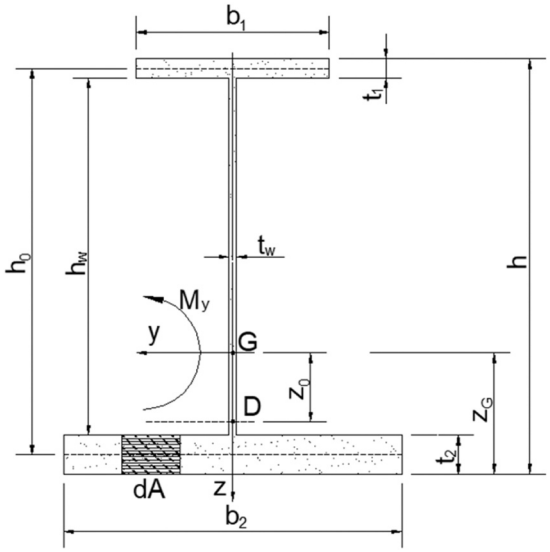

Fig. 1. Typical mono-symmetric I-section beam.

$$EI_z v_D^{IV} \pm M_y \theta'' = 0 \tag{1}$$

$$EC_w \theta^{IV} - \left(\pm 2M_y \beta_z + GJ\right)\theta'' - \left(\pm M_y - Nz_0\right) v_D'' = 0 \tag{2}$$

where v_D is the lateral displacement of the torsion center and θ is the twist rotation. By convention, M_y is positive when the part of the cross-section located at $z > 0$ is in tension. Considering fork boundary conditions and sinusoidal solutions for v_D and θ, Eqs. (1) and (2) become:

$$N_{cr,z}\left(N_{cr,x} r_0^2 \pm 2M_y \beta_z\right) - {M_y}^2 = 0 \rightarrow$$

$${M_y}^2 \pm 2M_y N_{cr,z} \beta_z - N_{cr,x} N_{cr,z} r_0^2 = 0 \tag{3}$$

where $N_{cr,z}$ is the elastic flexural buckling load about the z-axis and $N_{cr,x}$ is the elastic torsional buckling load. Finally, the solution for the system of Eq. (3), $M_y = M_{cr}$, is given by:

$$M_{cr} = \frac{\pi^2 EI_z}{L^2}\left\{\sqrt{\frac{C_w}{I_z} + \frac{L^2 GJ}{\pi^2 EI_z} + {\beta_z}^2} \pm \beta_z\right\} \tag{4}$$

where β_z is a factor that incorporates the Wagner effect [10] due to the mono-symmetry, given by:

$$\beta_z = z_0 - \frac{1}{2I_y}\int_A \left[z\left(y^2 + z^2\right)\right] dA \tag{5}$$

Conventionally, β_z is positive when the flange with the larger value of I_z is in compression at the point of largest bending moment.

For uniform members with variable boundary conditions and arbitrary loading, Eq. (6) gives a general expression for the elastic critical moment:

$$M_{cr} = C_1 \frac{\pi^2 EI_z}{\left(K_z L\right)^2}\left\{\sqrt{\left(\frac{K_z}{K_x}\right)^2 \frac{C_w}{I_z} + \frac{\left(K_z L\right)^2 GJ}{\pi^2 EI_z} + \left(\pm C_2 z_g \pm C_3 \beta_z\right)^2} - \left(\pm C_2 z_g \pm C_3 \beta_z\right)\right\} \tag{6}$$

where K_z and K_x are the effective length factors concerning flexural buckling about z-axis and torsional buckling, respectively; C_1, C_2 and C_3 are factors depending on the loading and end restraint conditions; and z_g is the distance between the point of load application and the torsion center, being positive for loads acting towards the torsion center from their point of application.

Table 1
Geometric properties for a mono-symmetric I-section.

$$z_G = \frac{b_2 \frac{t_2^2}{2} + h_w t_w \left[\frac{h_w}{3} + t_2\right] + b_1 t_1 \left(h - \frac{t_1}{2}\right)}{\left(b_1 t_1 - b_2 t_2\right) + h_w t_w} \tag{7}$$

$$z_0 = \frac{\left(z_G - \frac{t_2}{2}\right) t_2 b_2^3 - \left(h - z_G - \frac{t_1}{2}\right) t_1 b_1^3}{t_1 b_1^3 + t_2 b_2^3} \tag{8}$$

$$\beta_z = z_0 - \frac{1}{2I_y}\left\{\begin{array}{c} b_2 \frac{t_2}{4}(2z_G - t_2)\left(\frac{b_2^2}{6} + 2z_G^2 - 2z_G t_2 + t_2^2\right) + \\ \frac{t_w}{4} h_w (2z_G + t_2 - h - t_1)\left[\frac{t_w^2}{6} + (t_1 - z_G)^2 + (h - z_G - t_2)^2\right] + \\ b_1 \frac{t_1}{4}[t_1 - 2(h - z_G)]\left[\frac{b_1^2}{6} + (h - z_G - t_1)^2 + (h - z_G)^2\right] \end{array}\right\} \tag{9}$$

$$C_w = \frac{h_0^2}{12}\left(\frac{t_1 b_1^3 t_2 b_2^3}{t_1 b_1^3 + t_2 b_2^3}\right) \tag{10}$$

Table 1 summarizes some equations for determining the geometric properties of a mono-symmetric I-section: the centroid position (z_G – see Fig. 1), the torsion center coordinate (z_0 – see Fig. 1), the Wagner factor (β_z) and the warping constant (C_w).

.

2.2. A brief review of research on mono-symmetric I-sections and non-prismatic beams

The effect of mono-symmetry on the critical buckling moment of singly symmetric I-section beams was investigated by Kitpornchai and Trahair [11] in the beginning of the 1980 s. The authors derived approximations for the relevant cross-section properties to calculate the elastic critical moment, proposed new rules for design and compared them to results from different codes. In 1985, Roberts and Burt [12] studied the lateral-torsional buckling of mono-symmetric I-beams and cantilevers under uniform moment, distributed and concentrated loads using a general energy method derived by Roberts and Azizian [13]. The method is based on vanishing the second variation of the total potential energy and it guarantees that the influence of pre-buckling displacements is included in the analysis by incorporating strains, which stemmed from nonlinear expressions developed by Roberts [14]. The authors derived closed-form solutions for defining elastic critical loads of simply supported beams, which were proven valid for a wide range of cross-sections but overestimating certain cases. Wang and Kitpornchai [15] continued the work by extending the formulation for different load scenarios. Furthermore, the influence of intermediate restraints was studied by Wang et al. [16].

Earlier, Vlasov [9] and Goodier [17] obtained solutions for simply-supported I-beams with mono-symmetric cross-sections, but only subjected to uniform moment, and Anderson and Trahair [18] discussed the shortage of information available in the literature until the 1960 s, including previous solutions and differences of opinion on the effects of the mono-symmetry. They developed numerical solutions for mono-symmetric I-beams and cantilevers using differential equations, considering central concentrated loads for beams, end concentrated loads for cantilevers, and uniformly distributed loads, which were applied at several distances from the shear center. In the end, the authors concluded that the influence of the mono-symmetry and the distance from the point of application of the load to the shear center are beneficial for the critical loads of simply supported beams, and detrimental for cantilevers.

Several tables, charts and approximate expressions concerning the critical buckling of mono- symmetric I-section members were proposed by the aforementioned studies ([9–18]), until the beginning of 2000 s. The 3-factor formula developed by Clark and Hill [19], which was one of

the most common general formulations to predict the elastic critical moment hitherto, was included in the ENV version of Eurocode 3 [20]. However, two aspects were missing: the influence of the warping restraint condition on the elastic lateral torsional buckling of mono-symmetric I-section members and the extension of the domain of application of the 3-factor formula to cantilever members. In 2007, Andrade et al. [21] proposed expressions for each factor of Eq. (6) for cantilevers with equal or unequal flanges, fully built-in or free to warp at the ends and submitted to uniformly distributed or concentrated loads. In 2012, Camotim et al. [22] explained the interesting fact of the lowest critical bending moment is not necessarily related to the case of uniform bending for mono-symmetric I-section beams. From numerous numerical examples performed using the software LTBeam [23], it was proven that beams submitted to bending moment diagrams from transverse loads benefit the least from the cross-section asymmetry, which may lead to critical moments below to the ones associated to the uniform bending.

Non-linear phenomena associated with the stability of beams with mono-symmetric I-section were investigated ([24–27]). Mohri et al. [25] extended the available solutions developed for non-linear stability, studying the lateral buckling of beams in case of moment gradient applied at the extremities of the beam, considering large displacements and pre-buckling deflections. Trahair [26] investigated uniform and non-uniform bending and compared with available design recommendations, observing divergences between the numerical and analytical results. By these investigations, it was proven that the lateral buckling resistance depends not only on pre-buckling deformation, but also on section shape, load distribution, and if the largest flange is under compression or tension.

Recently, experimental tests and numerical simulations ([28–31]) have also been dedicated to study the ultimate resistance of mono-symmetric I-section beams made with high strength steels, evaluating the influence of initial geometric imperfections and residual stresses, in order to improve the current design rules.

Tapered beams with thin-walled I-sections are commonly applied due to their efficiency under bending and easy fabrication, and the use of mono-symmetric cross-sections can be advantageous for the resistance, mainly when the area of the flange under compression is increased. Bradford and Kuk [32] and Andrade and Camotim [33] addressed the elastic critical buckling moment of tapered mono-symmetric I-beams. Andrade et al. [34] discussed the use of beam or shell elements in the modeling of tapered mono-symmetric beams and Cockalingam et al. [35] proposed an improved Timoshenko beam formulation for the in-plane behavior of tapered mono-symmetric beams.

As tapered beams are used to be assumed with similar behavior as uniform beams, which can lead to inaccurate shear stress distributions, Trahair and Ansourian [36] studied the distributions of normal and shear stresses to mono-symmetric tapered I-beams considering inclined stress trajectories along the member instead of the methods commonly applied so far, in which plane sections are supposed to continue plane, shear strains are not considered when analyzing the bending deflections and stress concentrations are neglected. Comparing to finite element analysis, the authors concluded that their method could predict more accurate solutions to the transverse shear stresses. Trahair [37],[38] proposed a method to analyze tapered mono-symmetric I-section beams related to the elastic in-plane bending and out-of-plane flexural-torsional buckling based on numerical integration [37] and the elastic lateral buckling using the energy method [38] instead of closed forms commonly applied for uniform elements. An arbitrary axis system associated to the web mid-line was considered to avoid problems related to the variations of the centroid and shear center axes along the members. A computer program was written and validated to investigate the behavior of uniform beams, tapered doubly and mono-symmetric beams, beam-columns, and tapered cantilevers under different load and boundary conditions. The method developed showed to be efficient with rapid convergence and good approximated solutions since there is no need to consider many elements to obtain an accurate solution, as it is required when replacing tapered elements by many uniform elements.

Recently, Abdelrahman et al. [39] proposed generalized line-element formulations for geometrically nonlinear analysis of nonsymmetric tapered steel members. The element stiffness matrix was derived through the total potential energy, where elastic strains, as well as the warping deformations and the Wagner effects, were considered. Consequently, appropriate equations for the geometric parameters reflecting the variable geometry along the member were developed. In summary, average values of area, torsional rigidity, shear center coordinates, and Wagner coefficients are utilized in the element formulation, considering certain number of interval points along the length of the member. Although the method is validated for various cases, the validation included only tapered members. Furthermore, the element formulation involves incremental-iterative procedures, which may not be currently applicable by designers when confronted to more simplified methods that already exist.

Marques et al. [40] highlighted that the stability verification of tapered beams presents several inconsistencies and difficulties. Based on the new method for double-symmetric prismatic I-sections developed by Taras and Greiner [5], Marques et al. [40] derived a second-order analytical model using an Airton-Perry approach for web-tapered doubly symmetric beams and a generalized imperfection, which provided excellent agreement with experimental tests and was further validated by a large parametric study. Finally, Tankova et al. [8] developed a General Formulation for the stability design of steel columns, beams, and beam-columns with variable geometry, loads and different support conditions. However, the proposed approach was not extended for mono-symmetric I-section members, but it serves as the basis for the proposed methodology in this paper.

2.3. Design procedures for mono-symmetric I-beams

2.3.1. Eurocode 3

In EC3–1-1, the General Case (Clause 6.3.2.2) must be applied for uniform mono-symmetric beams. For non-prismatic, including tapered mono-symmetric beams, the General Method (Clause 6.3.4) must be applied.

According to the General Case, the reduction factor for lateral-torsional buckling (χ_{LT}), is given by:

$$\chi_{LT} = \frac{1}{\Phi_{LT} + \sqrt{\Phi_{LT}^2 - \overline{\lambda}_{LT}^2}} \tag{11}$$

where Φ_{LT} is obtained by:

$$\Phi_{LT} = 0.5\left[1 + \alpha_{LT}(\overline{\lambda}_{LT} - 0.2) + \overline{\lambda}_{LT}^2\right] \tag{12}$$

and the relative slenderness for lateral torsional buckling, $\overline{\lambda}_{LT}$, should be determined from:

$$\overline{\lambda}_{LT} = \sqrt{\frac{W_y f_y}{M_{cr}}} \tag{13}$$

in which W_y is the appropriate section modulus obtained according to the classification of the cross section, and M_{cr} is the elastic critical moment for lateral-torsional buckling. For welded I-sections, EC3–1-1 recommends curve *c* (imperfection factor - $\alpha_{LT} = 0.49$) for sections with $h/\min(b_1; b_2) \leq 2$, and curve *d* ($\alpha_{LT} = 0.76$) in the cases where $h/\min(b_1; b_2) > 2$.

According to the General Method, the reduction factor for lateral and lateral-torsional buckling (χ_{op}) can be obtained by Eq. (11), by adopting curve *c* for α_{LT} and replacing $\overline{\lambda}_{LT}$ in Eqs. (11) and (12) by:

$$\overline{\lambda}_{op} = \sqrt{\frac{\alpha_{ult,k}}{\alpha_{cr,op}}} \tag{14}$$

where $\alpha_{ult,k}$ is the minimum amplifier of the design load reaching the characteristic resistance of the most critical cross section of the beam, without taking lateral or lateral torsional buckling into account, and $\alpha_{cr,op}$ is the minimum amplifier of the design loads to reach the elastic lateral-torsional buckling of the beam.

2.3.2. AISC 360

The bending moment resistance of mono-symmetric I-section beams is given in Chapter F of AISC 360 [41], where the buckling curve is divided into three ranges: plastic, elastoplastic and purely elastic. Thus, the lateral-torsional buckling resistance is given (without partial factors), $M_{R,anal.}$, by:

$$M_{R,anal.} = \begin{cases} M_{pl}, \text{for} \lambda \le \lambda_p \\ C_b \left[M_{pl} - \left(M_{pl} - 0.7 f_y W_{el,y,c} \right) \dfrac{\lambda - \lambda_p}{\lambda_r - \lambda_p} \right] \le M_{pl}, \text{for} \quad \lambda_p < \lambda \le \lambda_r \\ M_{cr} \le M_{pl}, \text{for} \lambda > \lambda_r \end{cases} \tag{15}$$

where λ is the ratio between the unbraced length and radius of gyration of the "T" section formed by the compressed flange and the compressed part of the adjacent web, in the elastic range, about the z-axis; λ_p is the limiting parameter for the limit state of yielding; λ_r is the limiting parameter for the limit state of inelastic lateral-torsional buckling; C_b is a factor depending on the bending moment diagram and cross-section geometry; and $W_{el,y,c}$ is the elastic modulus about the y-axis of the compressed part of the section.

For determining the buckling resistance of tapered members, the American code recommends the guide *Frame Design Using Web-Tapered Members, Steel Design Guide 25* [42]. Basically, the method consists of determining an equivalent uniform beam with the same first-order resistance and the same elastic critical load as the tapered beam, and then, following the guidance for uniform beams (Eq. (15)) applied to the equivalent beam.

2.3.3. Marques et al. [40] proposal for web tapered beams

Marques et al. [40] proposal for web-tapered beams is based on a linear interaction between the first- and second-order bending moment utilizations, leading to a maximum utilization at a certain location, denoted as the second-order failure location (x_c^{II}). This method was built with an Ayrton-Perry analytical model as reference, and can be given by:

$$\chi_{LT}\left(x_c^{II}\right) + \frac{\chi_{LT}\left(x_c^{II}\right)}{1 - \overline{\lambda}_{LT}^2\left(x_c^{II}\right)\chi_{LT}\left(x_c^{II}\right)} \left[\alpha_{LT}\left(\overline{\lambda}_z\left(x_c^{II}\right) - 0.2 \right) \right] \left(\frac{\overline{\lambda}_{LT}^2\left(x_c^{II}\right)}{\overline{\lambda}_z^2\left(x_c^{II}\right)} \right) \frac{\xi\left(-\delta''_{cr,h_{\min}}\left(x_c^{II}\right) \right) EI_z\left(x_c^{II}\right)}{N_{cr,z,Tap}} \left[\frac{1 + \frac{N_{cr,z,Tap}}{M_{cr,Tap}} \frac{h\left(x_c^{II}\right)}{2}}{1 + \frac{N_{cr,z,Tap}}{M_{cr,Tap}} \frac{h_{\min}}{2}} \right] = 1.0 \tag{16}$$

where $N_{cr,z,Tap}$ and $M_{cr,Tap}$ are the elastic critical force of the tapered column about the weak axis and the elastic critical bending moment of the tapered beam, respectively; $h_{\min}$ is the minimum cross section height; ξ is the weighing factor for the imperfection; and $\delta''_{cr,h_{\min}}$ is the second derivative of the lateral displacement of the critical mode at $h = h_{\min}$. The imperfection factor (α_{LT}) is given by:

$$\alpha_{LT} = 0.21 \sqrt{\frac{W_{y,el}\left(x_c^{II}\right)}{W_{z,el}\left(x_c^{II}\right)}} \le 0.64 \tag{17}$$

in which $W_{z,el}$ and $W_{y,el}$ are the values of the elastic section moduli about the minor and the major axes, respectively, at x_c^{II} - location.

Table 2
Buckling mode for beams.

Buckling mode	Applied loads	Critical loads	Critical mode shape component
LTB	M_y	$M_{cr,N} + N_{cr,NM}$	$v_{cr}(x) + \theta_{cr}(x)$

3. General formulation for mono-symmetric beams

The utilization ratio of a generic single member may be expressed by equating the total longitudinal stress, σ, due to first- and second-order forces, to the yield stress, f_y:

$$\frac{\sigma(x)}{f_y} = \frac{N(x)}{A(x)f_y} + \frac{M_y(x)}{W_y(x)f_y} + \frac{M_z(x)}{W_z(x)f_y} + \frac{M_y^{II}(x)}{W_y(x)f_y} + \frac{M_z^{II}(x)}{W_z(x)f_y} + \frac{M_w^{II}(x)}{W_w(x)f_y} \tag{18}$$

where $A(x)$ is the cross-section area, $W_y(x)$ and $W_z(x)$ are the section moduli relative to the y- and z-axes, respectively, and $W_w(x) = C_w(x)/w_{\max}(x)$ is the warping modulus at location x along the member. $W_z(x)$ and $W_w(x)$ is calculated for the compressed part of the section. For mono-symmetric sections, $w_{\max}$ is given by:

$$w_{\max} = \left(h(x) - z_G(x) \pm z_0(x) \right) \frac{b_{comp}(x)}{2} \tag{19}$$

where $z_G(x)$ is the position of the cross-section centroid measured from the top face of the largest flange (see Fig. 1); $z_0(x)$ is the distance between the centroid and the torsion center of the cross section (see Fig. 1); and b_{comp} is the width of the compressed flange. It is noted that for section classes 1 and 2 the plastic section moduli should be used. Then, provided the second order contributions can be determined, the buckling resistance may be verified for an appropriate number of locations along the member, as follows:

$$\frac{N(x)}{A(x)f_y} + \frac{M_y(x)}{W_y(x)f_y} + \frac{M_z(x)}{W_z(x)f_y} + \frac{M_y^{II}(x)}{W_y(x)f_y} + \frac{M_z^{II}(x)}{W_z(x)f_y} + \frac{M_w^{II}(x)}{W_w(x)f_y} \le 1.0 \tag{20}$$

The verification of a single member with variable geometry, boundary conditions, subject to arbitrary loading is done by verifying Eq. (20) at enough locations (n) along the member, akin to the verification of the cross-section resistance. At each position, the respective values of the first order axial force, $N(x)$, bending moments $M_y(x)$, $M_z(x)$, second order contributions obtained from the relevant buckling mode, and cross-section properties, $A(x)$, $I_z(x)$, etc. are to be used.

For prismatic members, all these buckling cases are covered by the Eurocode 3 design rules. The only condition is that the designer needs to choose the relevant buckling mode and the corresponding verification format (see Table 2).

For lateral-torsional buckling of mono-symmetric beams, considering Table 2, the general interaction (Eq. (18)) becomes:

$$\frac{\sigma(x)}{f_y} = \frac{M_y(x)}{W_y(x)f_y} + \frac{M_z^{II}(x)}{W_z(x)f_y} + \frac{M_w^{II}(x)}{W_w(x)f_y} \tag{21}$$

where there are two second-order contributions, the out-of-plane bending moment depending on the lateral displacement:

$$M_z^{II}(x) = -EI_z(x)v''(x) \tag{22}$$

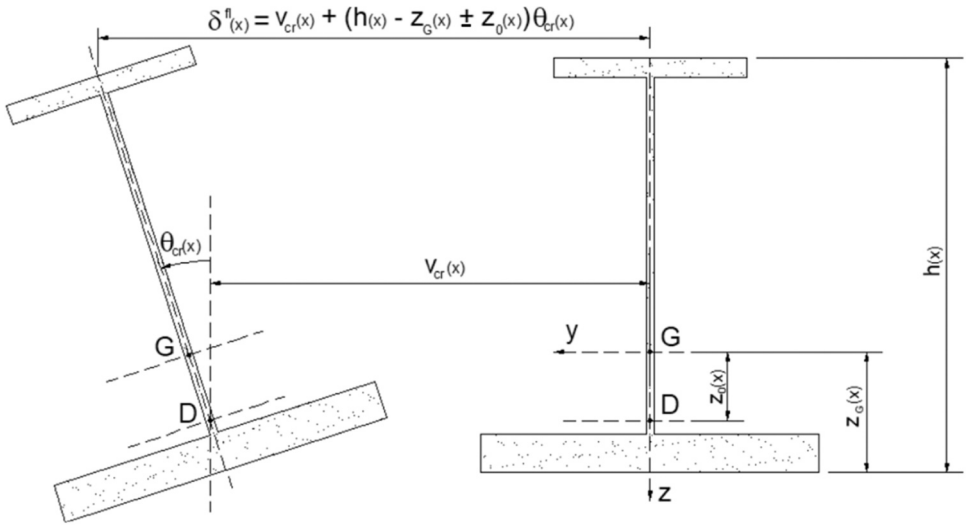

Fig. 2. General displacement of the critical mode.

and the bi-moment depending on the twist rotation:

$$M_w^{II}(x) = -EC_w(x)\left[\theta''(x) + \frac{W_w(x)}{W_z(x)}\frac{I_z(x)}{C_w(x)}\theta'(x)h'\right] \tag{23}$$

Hence, when considering the amplitude of the initial imperfection, both components (lateral displacement and twist rotation) must be considered. For simply supported beams it is possible to obtain the amplitude by the coupling of the lateral displacement and twist rotation [43]. In a more general configuration (variation of the geometry along the member, different boundary and loading conditions, etc.), this relationship may not hold. For that reason, it was chosen to use both components of the mode shape as initial imperfection, assuming that they are multiplied by the same amplitude:

$$v_0(x) = v_{cr}(x)\bar{\delta}_{0,LTB} \tag{24}$$

and

$$\theta_0(x) = \theta_{cr}(x)\bar{\delta}_{0,LTB} \tag{25}$$

where v_{cr} is the out-of-plane component and θ_{cr} is the twist rotation.

The resulting amplification relationship for the displacement and rotation is given by:

$$v(x) = \frac{1}{\alpha_{cr} - 1}v_0(x) \tag{26}$$

and

$$\theta(x) = \frac{1}{\alpha_{cr} - 1}\theta_0(x) \tag{27}$$

in which α_{cr} is the critical load multiplier.

It is assumed that the real beam should have the same resistance as an equivalent beam with fork supports and constant bending moment. This equivalent beam has the same geometry as the real beam at the critical cross-section and the same elastic critical moment. Hence, it is possible to obtain the required generalized imperfection by setting equal the second-order utilization for the equivalent and real beams. The second-order moments for a simply supported beam at mid-span are given by:

$$M_z^{II}(x_m) = M_{y,Ed}\theta_{tot} = M_{y,Ed}\theta_0\frac{1}{1 - 1/\alpha_{cr}} = \frac{\alpha_{cr}M_{y,Ed}(x_m)\bar{e}_0\theta_{cr}(x_m)}{\alpha_{cr} - 1} \tag{28}$$

$$M_w^{II}(x_m) = M_{y,Ed}v_{tot} - GJ\theta - 2M_{y,Ed}\beta_z\theta_{tot} =$$

$$M_{y,Ed}v_0\frac{1}{1 - 1/\alpha_{cr}} - GJ\left(\theta_0\frac{1}{1 - 1/\alpha_{cr}} - \theta_0\right) - 2M_{y,Ed}\beta_z\theta_0\frac{1}{1 - 1/\alpha_{cr}} =$$

$$\frac{\alpha_{cr}M_{y,Ed}(x_m)\bar{e}_0\theta_{cr}(x_m)}{\alpha_{cr} - 1}\left(\frac{v_0(x_m)}{\theta_0(x_m)} - \frac{GJ(x_m)}{M_{cr}} - 2\beta_z(x_m)\right) \tag{29}$$

The second order utilization ratio for the equivalent member is given by:

$$\begin{aligned}\varepsilon_M^{II}(x_m) &= \frac{M_z^{II}(x_m)}{W_z(x_m)f_y} + \frac{M_w^{II}(x_m)}{W_w(x_m)f_y} \\ &= \frac{\alpha_{cr}M_{y,Ed}(x_m)\bar{e}_0\theta_{cr}(x_m)}{W_z(x_m)f_y(\alpha_{cr} - 1)}\left(1 + \frac{v_{cr}(x_m)}{\theta_{cr}(x_m)}\frac{W_z(x_m)}{W_w(x_m)} + \frac{GJ(x_m)}{M_{cr}}\frac{W_z(x_m)}{W_w(x_m)}\right. \\ &\quad \left. + 2\beta_z(x_m)\frac{W_z(x_m)}{W_w(x_m)}\right) \\ &= \frac{N_{cr,TF}\bar{e}_0}{W_z(x_m)f_y(\alpha_{cr} - 1)}\end{aligned} \tag{30}$$

with

$$N_{cr,TF} = \alpha_{cr}M_{y,Ed}(x_m)\theta_{cr}(x_m)\frac{W_z(x_m)}{W_w(x_m)}\left(\frac{W_w(x_m)}{W_z(x_m)} + \frac{v_{cr}(x_m)}{\theta_{cr}(x_m)} + \frac{GJ(x_m)}{M_{cr}} + 2\beta_z(x_m)\right) \tag{31}$$

The second order utilization of the real beam at the location x_m is given by:

$$\varepsilon_M^{II}(x_m) = \frac{M_z^{II}(x_m)}{W_{z,comp}(x_m)f_y} + \frac{M_w^{II}(x_m)}{W_{w,comp}(x_m)f_y} = \frac{EI_z(x_m)}{W_{z,comp}(x_m)f_y(\alpha_{cr} - 1)}\left[v'_{cr}(x_m) + \frac{W_{z,comp}(x_m)}{W_{w,comp}(x_m)}\frac{C_w(x_m)}{I_z(x_m)}\left(\theta''_{cr}(x_m) + \frac{W_{w,comp}(x_m)}{W_{z,comp}(x_m)}\frac{I_z(x_m)}{C_w(x_m)}\theta'_{cr}(x_m)h'\right)\right]\bar{\delta}_0 \tag{32}$$

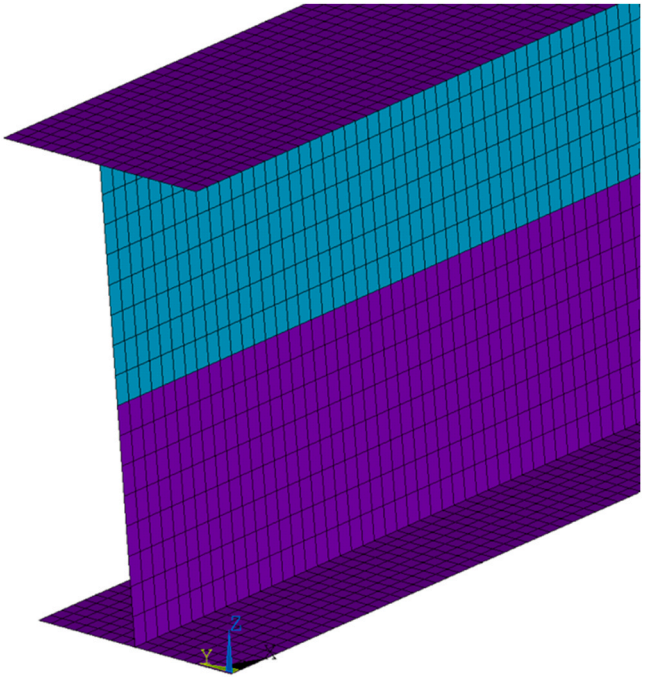

Fig. 3. Representation of the mesh for an I-section member.

Equaling the second order utilization ratio for the equivalent beam and the real beam at the location x_m leads to the following expression for the amplitude of the imperfection:

$$\bar{\delta}_{0,LTB} = \frac{N_{cr,TF}\bar{e}_0}{EI_z(x_m)\left[v''_{cr}(x_m) + \frac{W_z(x_m)}{W_w(x_m)}\frac{C_w(x_m)}{I_z(x_m)}\left(\theta''_{cr}(x_m) + \frac{W_w(x_m)}{W_z(x_m)}\frac{I_z(x_m)}{C_w(x_m)}\theta''_{cr}(x_m)h'\right)\right]} = f_\eta \bar{e}_0 \tag{33}$$

This amplitude is used with the proposed generalization. It contains the equivalent geometrical imperfection $\bar{e}_0$ but also additional terms ensuring consistency with the Eurocode 3 design rules. Ideally, x_m should be chosen as the correct critical location. To avoid an iterative procedure, the location x_m is adopted where $|v'_{cr}(x)|$ reaches a maximum. The amplitude of the generalized imperfection is given by:

$$\eta^*(x) = \alpha_{LT}(x)(\bar{\lambda}(x) - 0.2)f_\eta|\delta^{fl}(x)|\frac{W_z(x)}{A(x)} \tag{34}$$

where $\alpha_{LT}(x)$ is calculated according to FprEN 1993–1-1 prescriptions for lateral-torsional buckling of welded prismatic members, and

$$f_\eta = \frac{N_{cr,TF}}{EI_z(x_m)\left[v''_{cr}(x_m) + \frac{W_z(x_m)}{W_w(x_m)}\frac{C_w(x_m)}{I_z(x_m)}\left(\theta''_{cr}(x_m) + \frac{W_w(x_m)}{W_z(x_m)}\frac{I_z(x_m)}{C_w(x_m)}\theta''_{cr}(x_m)h'\right)\right]} \tag{35}$$

For mono-symmetric I-sections, the general displacement of the critical mode, $\delta^{fl}(x)$, is given by a geometric relationship between the lateral displacement and the section rotation, as defined by Eq. (36) and Fig. 2:

$$\delta^{fl}(x) = v_{cr}(x) + (h(x) - z_G(x) \pm z_0(x))\theta_{cr}(x) \tag{36}$$

Thus, the final verification equation is given by:

$$\varepsilon_M(x) = \frac{M_{y,Ed}(x)}{W_y(x)f_y} + \frac{EI_z(x)\left[v''_{cr}(x) + \frac{W_z(x)}{W_w(x)}\frac{C_w(x)}{I_z(x)}\left(\theta''_{cr}(x) + \frac{W_w(x)}{W_z(x)}\frac{I_z(x)}{C_w(x)}\theta''_{cr}(x)h'\right)\right]}{A(x)f_y(\alpha_{cr} - 1)}\eta(x) \leq 1.0 \tag{37}$$

with

$$\eta(x) = \alpha_{LT}(x)(\bar{\lambda}(x) - 0.2)f_\eta|\delta^{fl}(x)| \tag{38}$$

An equivalent elastic critical force $N_{cr,TF,eq.}$ is "retrieved" from the buckling mode using the differential equation for flexural buckling:

$$EI_z(x)v''_{cr}(x) - N_{cr,TF}v_{cr}(x) - z_0N_{cr,TF}\theta_{cr}(x) = 0. \tag{39}$$

Then, the equivalent force becomes:

$$N_{cr,TF,eq} = \frac{EI_z(x_m)|v''_{cr}(x_m)|}{|v_{cr}(x_m) + z_0\theta_{cr}(x_m)|} \tag{40}$$

It is this force that is used for the calculation of the normalized slenderness:

$$\bar{\lambda}(x) = \sqrt{\frac{A(x)f_y}{N_{cr,TF,eq}}}. \tag{41}$$

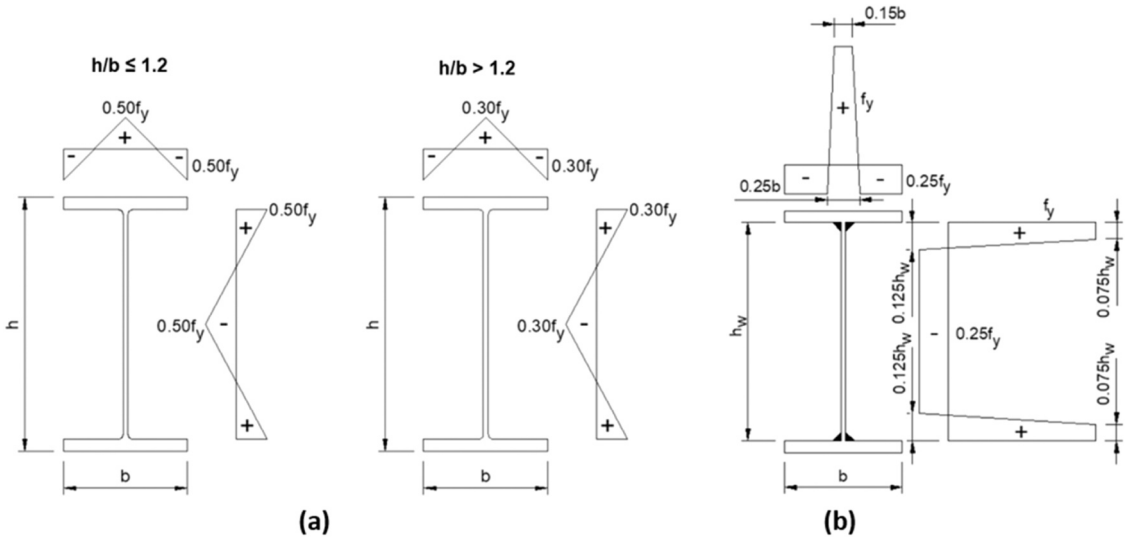

Fig. 4. Pattern of residual stresses for (a) hot-rolled and (b) welded I-sections, recommended by ECCS [46].

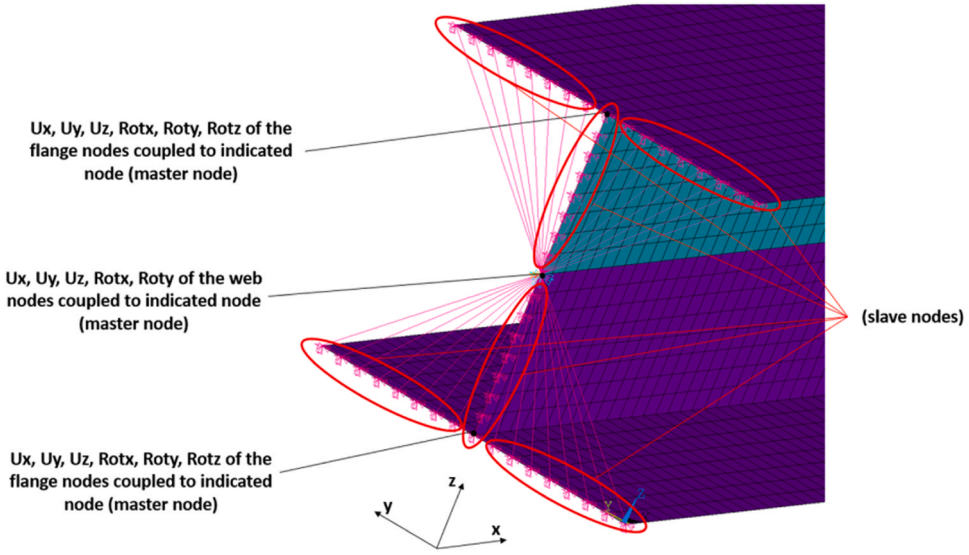

Fig. 5. Kinematic coupling constraints for the cross-sections of the end extremities of the numerical beam model.

4. Numerical modeling

4.1. Description of the numerical model

The numerical analyses were performed using the finite element software ANSYS (version 22.0) [44]. The geometry of the models was defined using the nominal dimensions of the cross-sections. The SHELL181 element, which is composed by 4 nodes with 6 degrees of freedom per node, was chosen to discretize the mesh. After a mesh sensitive study, 16 elements were defined across the flange's width and 16 across the web's depth (see Fig. 3), in agreement with previous studies [45]. The same size of the elements across the width and depth was used along the length of the member, generating only quadratic elements (see Fig. 3).

Geometrically and materially nonlinear analyses with imperfections (GMNIA) were executed to obtain the ultimate resistance of the numerical models by using the arc-length method and the von Mises failure criterion. Initial geometric imperfections were introduced with a shape corresponding to the first buckling mode obtained from previous linear buckling analyses (LBA). The validation models were run considering the measured material stress-strains curves, residual stress diagrams and amplitude of the initial geometrical imperfections obtained from experimental works found in the literature. In the parametric study, following ECCS [46] recommendations, an amplitude of imperfection equal to $L/1000$ and the ECCS pattern of residual stresses for welded I-sections (see Fig. 4-a) were implemented in the numerical models. The constitutive law was adopted according to Yun and Gardner [47] as true stress-strain curve for the parametric study, which is representative of hot-rolled steels with a yield plateau and strain hardening and was recently included in prEN 1993–1-14 [48].

To simulate fork boundary conditions, the validated boundary conditions adopted by Snijder et al. [49] (see Fig. 5) are utilized. On both end extremities of the beam, all nodes of top flanges (namely slave nodes - see Fig. 5) are coupled for all their displacements (Ux, Uy, and Uz) and rotation (ROTx, ROTy, and ROTz) to the node located at the middle of this flange (indicated node – namely master node) by using kinematic coupling constraints, and the same is applied to the bottom flange. This makes the flange infinitely rigid. For the web, all nodes (namely slave nodes - see Fig. 5) are coupled for all their displacements (Ux, Uy, and Uz) and rotations about *x* and *y* (ROTx and ROTy – see Fig. 5) to the node located in the middle of the web (indicated node – namely master node). As result of these constraints, the sections at extremities are infinitely rigid and can warp. Secondly, for fixing the numerical model, boundary conditions are applied at the node located in the middle of the web. In one of the ends of extremities, the displacements Ux, Uy, Uz and the rotation ROTx of this node are restricted, and in the other one, only Uy, Uz, and ROTx are zero. The end bending moments are applied at the same node where the boundary conditions are implemented.

4.2. Numerical model validation

4.2.1. Introduction

The numerical model was validated using the experimental test results from Tankova *et al.* [28] and Lebastard [50]. Additionally, available numerical benchmarks by Tankova *et al.* [28] for uniformly distributed loads (DL) and linearly varying bending moments (LBM) were used to cover loading cases that were not covered by the experimental tests that were both implemented with concentrated loads.

4.2.2. Experimental results by Tankova et al. [28]

The experimental model of Tankova *et al.* [28] is a four-point

Fig. 6. Numerical Models based on experimental tests by Tankova et al. [28].

Table 3
Experimental parameters from Tankova et al. [28] used in the numerical model validation.

Prototype	Member	$\bar{\lambda}_{LT}$	Fab.	Steel grade		Section classification	Amplitudes of Geometrical Imperfections (mm)*	
				Flanges	Web		In-plane	Out-of-plane
B11	700 ×200(400) X 8 × 16	1.01	Welded	S690	S690	4	0.96	0.34
B12		1.00		S690	S355		0.07	4.48
B13		0.84		S460	S460		1.31	0.90
B14		0.83		S460	S355		1.93	1.29

* Measurements at mid-span.

Table 4
Material properties measured by Tankova et al. [28] and used in the numerical model validation.

Plate/ Thickness	Steel grade	E (GPa)	f_y (MPa)	f_u (MPa)	Ultimate strain (%)
8 mm	S355	202.6	425.5	634.7	12.2
8 mm	S690	200.4	755.3	813.0	6.2
16 mm	S690	204.0	798.4	854.8	5.9
8 mm	S460	212.5	528.8	639.2	11.0
16 mm	S460	201.1	498.9	656.2	9.4

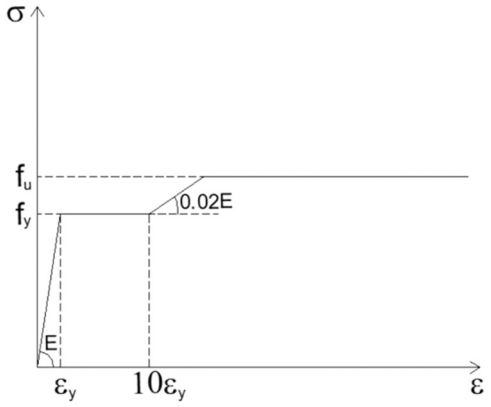

Fig. 7. Constitutive material law adopted in the numerical model validation.

Table 5
Experimental and numerical results for P_{ult}, considering experimental results from Tankova et al. [28].

Prototype	$P_{ult}(kN)$		Num./Exp.
	Experimental	Numerical	
B11	1731.8	1732.0	1.00
B12	1601.0	1610.9	1.01
B13	1307.2	1301.1	1.00
B14	1133.3	1210.0	1.07

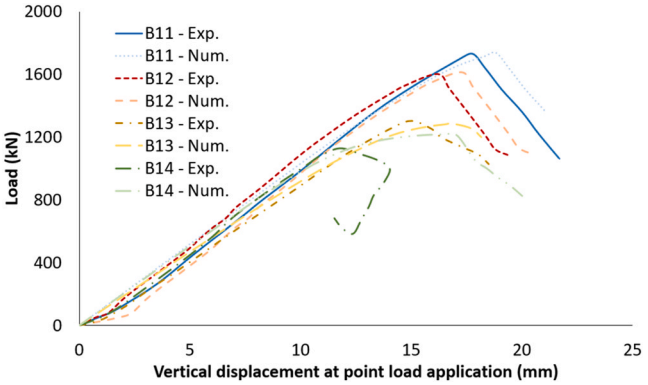

Fig. 9. Load-vertical displacement curves – displacements measured at point load application.

bending model where the vertical forces are applied at two locations, as shown in Fig. 6. 16 mm-thickness stiffeners are considered at extremities and at the locations where the vertical forces were applied. Fork-support conditions are considered at the extremities, with additional lateral restraints at the location of the vertical forces (see Fig. 6). All prototypes are 6 m long, with an unbraced distance between the vertical forces equal to 4 m. The main parameters of the mono-symmetric I-section beams are shown in Table 3. All prototypes have identical cross-section, but fabricated from different steel grades: S460, S690 and hybrid. The geometrical imperfections exhibited in Table 3 were measured using an

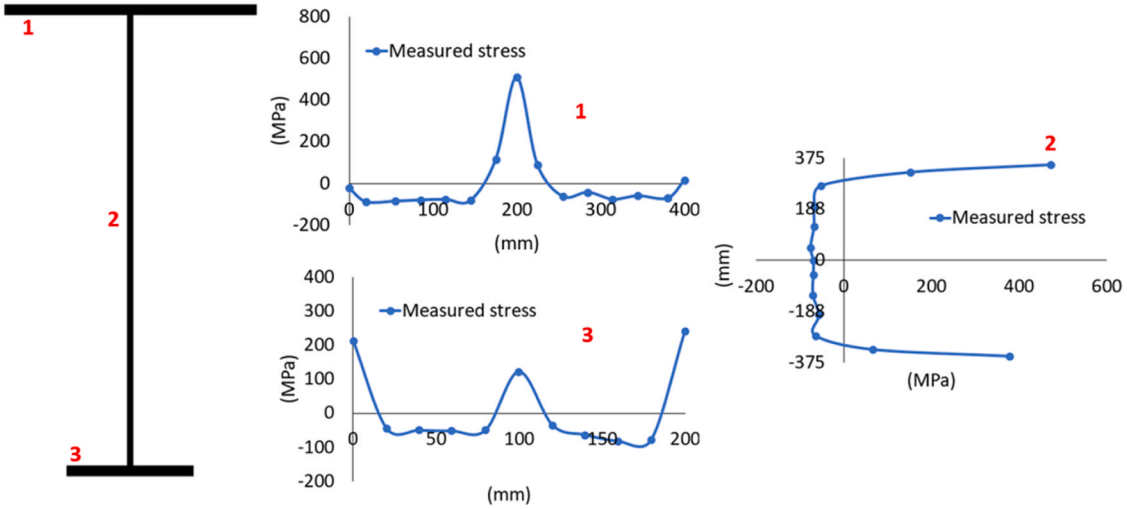

Fig. 8. Residual stress measured by Tankova et al. [28] for prototype B11 and adopted in the numerical model validation.

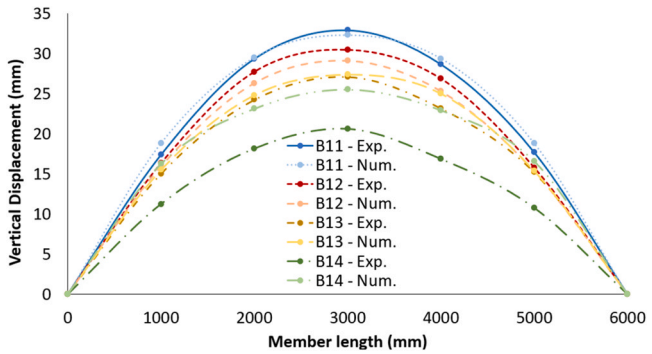

Fig. 10. Vertical displacements at maximum load – displacements measured at bottom flange.

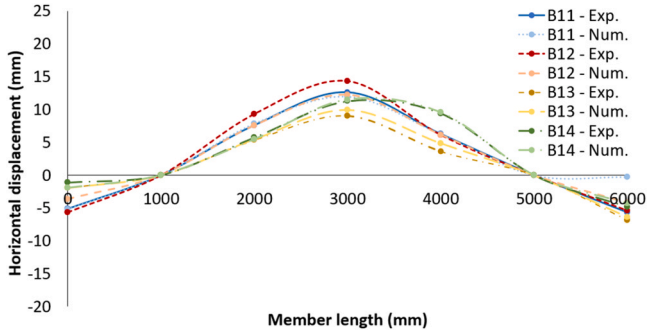

Fig. 11. Horizontal displacements at maximum load – displacements measured at the middle of the web.

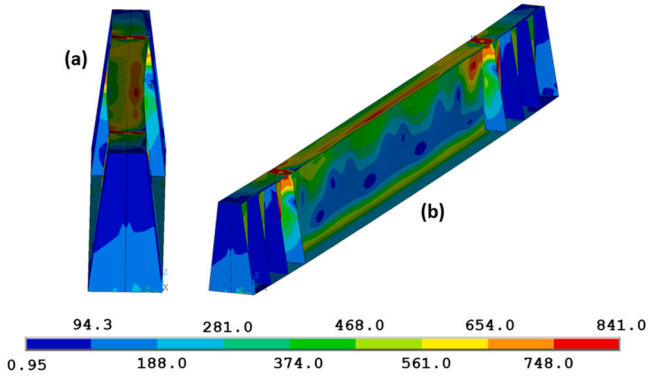

Fig. 12. von Mises stress distribution (in MPa) relative to the ultimate load capacity of the numerical model B11 – (a) longitudinal view; (b) perspective view.

optical 3D scan system.

Table 4 presents the measured material properties from the plates that make up each section shown in Table 3 that were included in the numerical models according to the constitutive law shown in the Fig. 7, which was also adopted in the numerical analyses of Tankova et al. [28].

Fig. 8 shows the measured residual stresses obtained from prototype B11 (see Table 3) and implemented in the numerical models. The diagrams shown in this figure was applied in all the numerical model validation.

Table 5 and Figs. 9–11 compare the experimental and numerical results. There is excellent agreement between numerical and experimental results, both in terms of stiffness and ultimate resistance. It is noted that the larger differences for B14 test may be attributed to the fact that there was no measurement of residual stresses for this cross-section. All numerical models failed by lateral-torsional buckling, in line with the experimental results, as depicted in Fig. 12.

4.2.3. *Experimental results by Lebastard [50]*

The experimental work by Lebastard [50] included lateral-torsional buckling tests on two uniform and two tapered members, one having a mono-symmetric cross-section while the other is doubly symmetrical within each of the groups. The test set up of the four 8.43 m long beams was similar. The load was applied at the top flange of a laterally restrained cross-section located at 2.18 m from one of the extremities of the member (see Fig. 13). Fork support conditions were imposed at both end extremities. On both sides of the web, 30 mm-thick transverse stiffeners were placed at the three laterally restrained cross-section. Besides, a 20 mm-thick longitudinal stiffener was positioned on both sides of the web along the 2.18 m-long segment (see Fig. 13), and thus, the unbraced length was 6.25 m. The nominal dimensions and material of the tested members, as well as the measured amplitudes of the geometrical imperfections, are given in Table 6. Note that, unlike the prototypes from Tankova et al. [28], where the sections have flanges with different widths and equal thicknesses (see Table 3), the mono-symmetry of the sections shown in Table 6 is due only to the difference in thickness of the flanges, which have the same width. Furthermore, it is noteworthy that the bending moment diagrams of these two experimental works are different: constant bending moment in Tankova et al. [28] and triangular-diagram in Lebastard [50] within the unbraced lengths.

Fig. 14 presents the material laws for each plate thickness and implemented in the numerical model. Each material law corresponds to the true stress-strain behavior relative to results of coupon tests performed by Lebastard [50]. Fig. 15 presents the residual stress diagram measured by Lebastard [50] for each prototype shown in Table 6 and adopted in the numerical simulations.

Table 7 and Figs. 16–18 compare the experimental and the numerical results. These comparisons show that the stiffness of the numerical models as well as their ultimate resistance are in good agreement with the experimental results. Similarly to the experimental prototypes, all numerical models failed by lateral-torsional buckling, as can be seen in Fig. 19, further evidencing the validity of the numerical model of this work.

4.2.4. *Numerical benchmarks*

The calibrated numerical models conducted by Tankova et al. [8] present the following features:

(i) hot-rolled double symmetric sections, steel grade S235 and Class 1;
(ii) fork boundary conditions at the end extremities;
(iii) uniformly distributed loads in the z-direction or linearly varying end bending moments;
(iv) no transverse or longitudinal stiffeners;
(v) initial geometric imperfections with an amplitude equal to $L/1000$ and with the hot-rolled residual stress pattern shown in Fig. 4-a, as recommended by ECCS [46].

Table 8 shows that both numerical models are practically coincident, presenting excellent agreement.

5. Validation of general formulation for mono-symmetric beams

5.1. *Parametric study*

Using the validated numerical model, a large parametric study on mono-symmetric welded I-beams is defined and performed. The results of this parametric study will be used to validate the proposed General Formulation for mono-symmetric I-sections (Section 3) and compare its results with the available design proposals. The parametric study is divided into two subsets as follows:

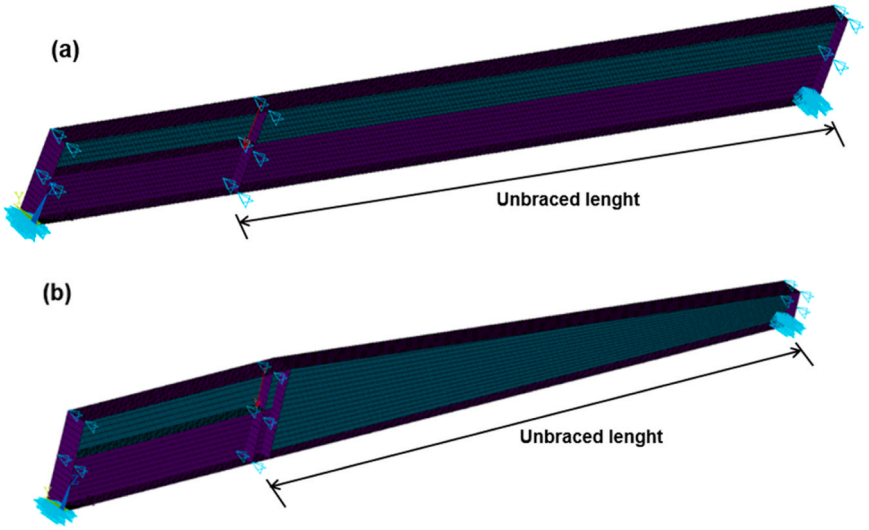

Fig. 13. Numerical Models based on experimental prototypes geometry of (a) uniform and (b) tapered members from Lebastard [50].

Table 6
Experimental parameters from Lebastard [50] used in the numerical model validation.

Prototype	Member	$\bar{\lambda}_{LT}$	Fab.	Steel grade	Section classification	Out–of-plane imperfections (mm)*
U-DS	804 × 200×8 × 20	0.74	Welded	S355	3	3.4
U-MS	804 × 200×8 × 20(15)					4.0
T-DS	(836 to 286) X 200 × 8×20					3.3
T-MS	(836 to 286) X 200 × 8×20(15)					5.0

* Amplitude of imperfection measured at the flange in compression.

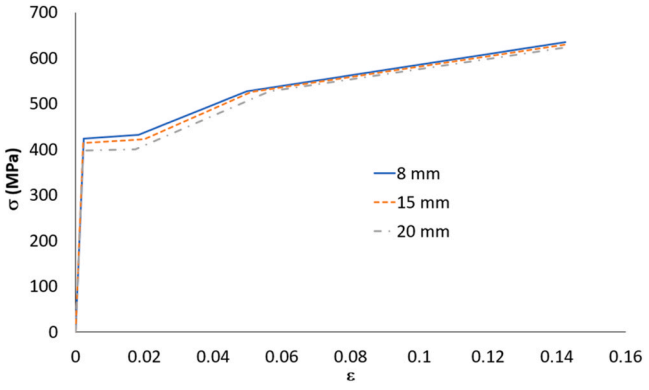

Fig. 14. Material law obtained by Lebastard [50] and implemented in the numerical model validation.

i. prismatic beams, subjected to linear bending moment, uniformly distributed loading and concentrated loads, with fork boundary conditions - see Table 9 –, totaling 1296 numerical models.

.

Table 10 summarizes the range of some parameters covered by the parametric study shown in Table 9. For the mono-symmetric beams, sections with flanges with the larger value of I_z in tension or in compression are analyzed separately. In this table, the ratios $z_G/(h/2)$ and $W_{y,el,\min}/W_{y,el,\max}$ show the level of asymmetry of the cross-section with respect to the *y*-axis, where $W_{y,el,\min}$ and $W_{y,el,\max}$ are respectively the minimum and maximum values of the elastic section moduli about the major axis. When the values of both ratios are equal to 1.0, the cross-section is doubly symmetric.

* See Fig. 1.

i. Tapered and non-prismatic S235 grade steel beams, with the largest flange in tension, and $\bar{\lambda}_z = 1.30$, comprising:

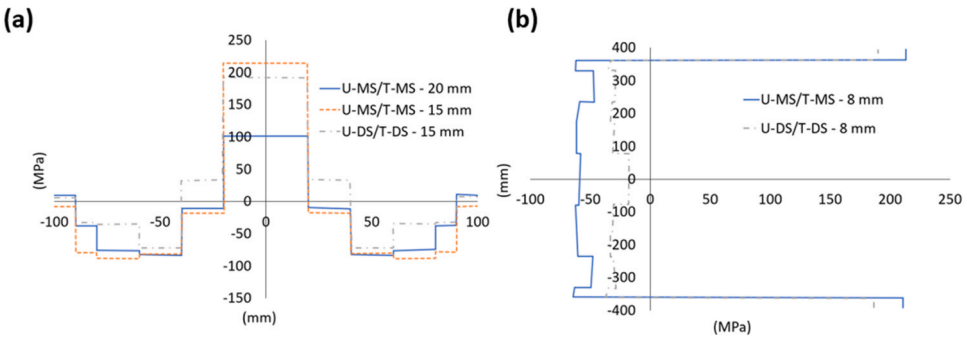

Fig. 15. Residual stress measured by Lebastard [50] and adopted in the numerical model validation – (a) flanges and (b) web.

Table 7
Experimental and numerical results for P_{ult}, considering experimental results from Lebastard [50].

Prototype	P_{ult} (kN)		Num./Exp.
	Experimental	Numerical	
U-DS	747.6	733.6	0.98
U-MS	903.6	887.3	0.98
T-DS	720.6	684.6	0.95
T-MS	775.8	726.3	0.94

(ii.a) mono- and doubly symmetric web-tapered members with only the largest flange inclined (for mono-symmetric sections); subjected to distributed load (TF, BF, G and D point loading application – point loading D only for mono-symmetric sections - Fig. 20) and constant bending moment (Fig. 21); three additional cases were studied: member with restraint at the flange in tension, located at mid-span; and at 1/3 and 2/3 of the length; and member with restraint at the flange in compression, located at mid-span (see Fig. 20 and Fig. 21). The following cross-sections are studied: h x 200(200) x 8 × 16(16), h x 300 (200) x 8 × 16(16), and h x 410(410) x 31 × 70(55), with maximum depth equal to 500, 500, and 1138, respectively. The ratio between the maximum and minimum depth of the tapered members is equal to 2.0 for all cases studied. Number of numerical models: 56.

(ii.b) parabolic and anti-parabolic members with mono-symmetric cross-sections (Fig. 22 and Fig. 23, respectively), subjected to distributed load (TF point loading application – Fig. 22 and Fig. 23). Additionally, the lateral restraints cases of (ii.a) subset were studied in this subset (see Fig. 22 and Fig. 23). The considered cross-sections at the end of the members are: 500 × 200(150) x 12 × 50(30), 750 × 180(250) x 15 × 35(25), 800 × 300(200) x 18 × 35(50), and 1138 × 410(410) x 31 × 70(55), and the cross-section at mid-span has the depth incremented or subtracted by a (Fig. 22 and Fig. 23), considering a/L equal to 0.05. The boundary conditions at the ends of the members of this subset are equal to those of subset (i), except for the in-plane rotation (rotation about the y-axis), where a rotation spring equivalent to about 50% of the clamped elastic critical bending moment is applied (see Fig. 22 and Fig. 23). Number of numerical models: 32.

The two subsets (ii.a) web-tapered and (ii.b) parabolic and anti-parabolic variation of the beam depth were chosen because they represent the two common practical cases. The specific choice of the cases followed a similar parametric study carried out by Tankova et al. [8] for doubly symmetric non-prismatic beams, thereby allowing for direct comparison.

The cross-sections of the end extremities of all numerical models (subsets (i) and (ii)) of the parametric study are modeled as shown in Fig. 5, adjusted to the appropriate loading and boundary conditions.

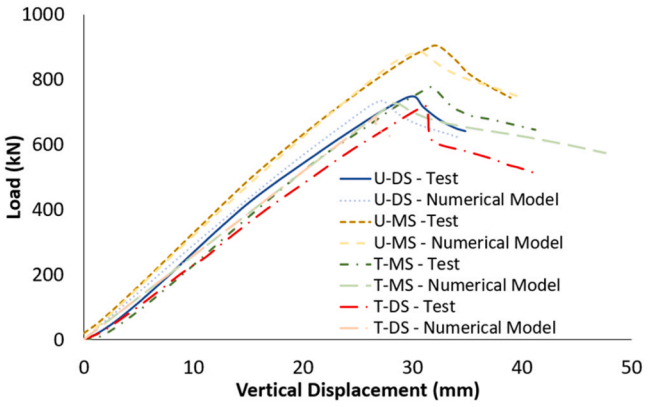

Fig. 16. Load-vertical displacement curves – displacements measured at top flange at 1.042 m from point load application (within buckling length).

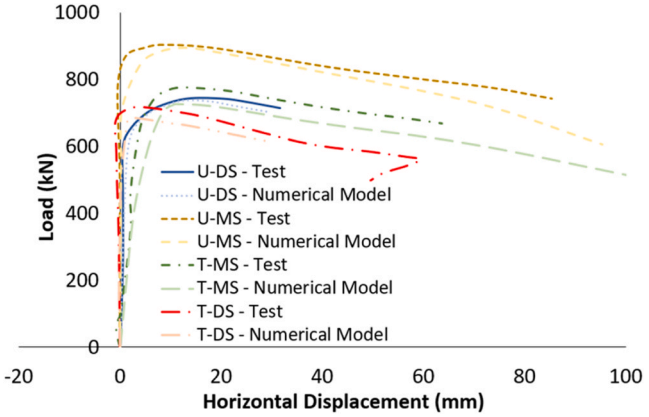

Fig. 17. Load-horizontal displacement curves – displacements measured at middle of the web at 1.042 m from point load application (within buckling length).

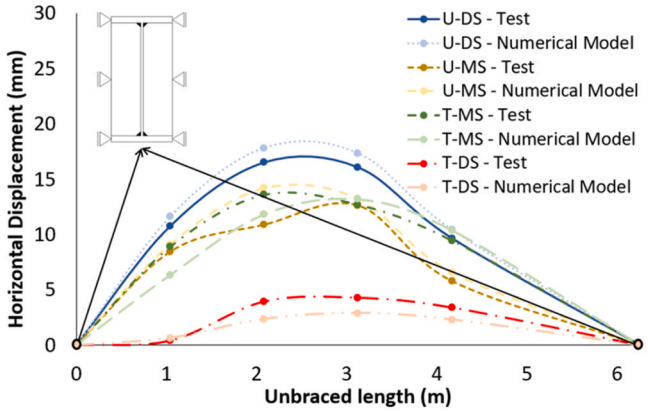

Fig. 18. Horizontal displacements at maximum load – displacements measured at middle of the web along the member.

5.2. Comparison between LBA and GMNIA deformed shapes

First, as the General Formulation relies on the second derivatives of the elastic critical buckling mode shape (v''_{cr} and θ''_{cr}), it is important to verify if the deformed shape of the first eigenvalue of LBA analysis are similar to the GMNIA results for the ultimate compressive load substep, for the correct application of the method. Fig. 24 compares the

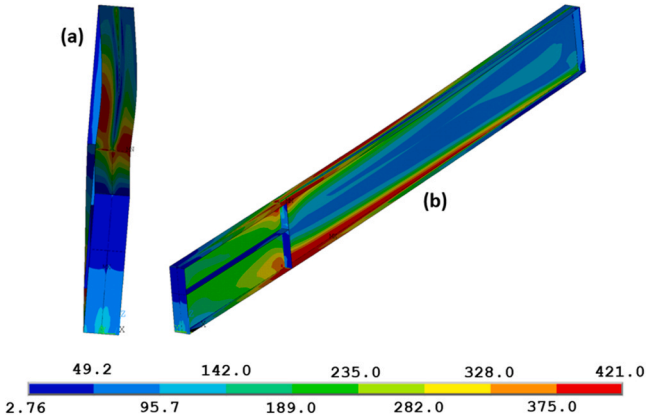

Fig. 19. von Mises stress distribution (in MPa) relative to the ultimate load capacity of the numerical model U-MS – (a) longitudinal view; (b) perspective view.

Table 8
Numerical parameters from Tankova et al. [8] used in the numerical model validation and comparison between both numerical results.

#	Section	L (m)	$\bar{\lambda}_z$	$\bar{\lambda}_{LT}$	Load	$\chi_{Tankova\ et\ al.[8]}$*	$\chi_{Num.Mod.}$*	$\frac{\chi_{Num.Mod.}}{\chi_{Tankova\ et\ al.[8]}}$
1	HBE200	9.68	2	0.77	LBM ($\psi = 0$)	0.999	1.000	1.00
2		14.52	3	0.96	LBM ($\psi = 0$)	0.945	0.926	0.98
3		7.26	1.5	0.82	DL	0.874	0.864	0.99
4	IPE300	6.40	2	0.84	LBM ($\psi = -1$)	0.936	0.943	1.01
5		9.60	3	1.08	LBM ($\psi = -1$)	0.724	0.709	0.98
6		4.80	1.5	1.05	DL	0.640	0.633	0.99

* Ratio between ultimate numerical bending moment and plastic bending moment.

Table 9
Parametric study for prismatic mono- and doubly symmetric cross-sections.

Section $h\ xb_2(b_1)xt_wxt_2(t_1)$	$\bar{\lambda}_z$	**Steel grade**	**Bending Moment diagram**	**Stress on the largest flange****
300 × 150(150) x 8 × 20(15) 300 × 150(150) x 8 × 30(20) 400 × 180(180) x 10 × 30(20) 400 × 180(180) x 10 × 40(25) 500 × 200(150) x 12 × 50(30) 400 × 180(180) x 10 × 30(30)*	0.50 to 5.0	S235 S355 S460	Linear ($\psi = 1.0$, 0.0 and −1.0)	Tension Compression
400 × 180(180) x 10 × 40(25) 500 × 200(150) x 12 × 50(30) 430 × 350(200) x 8 × 40(20) 400 × 180(180) x 10 × 30(30) *			Distributed load (applied at the top face -TF, the centroid - G, the torsion center - D*** and the bottom face - BF) Point load (applied at the top face -TF, the centroid - G, the torsion center - D*** and the bottom face - BF)	Tension
600 × 476(476) x 100 × 140(140) * 1138 × 410(410) x 31 × 55(55) * 600 × 476(350) x 100 × 140(140) 1138 × 410(410) x 31 × 70(55)			Linear ($\psi = 1.0$) Distributed load (applied at the top face -TF, the centroid - G, the torsion center - D*** and the bottom face - BF) Point load (applied at the top face -TF, the centroid - G, the torsion center - D*** and the bottom face - BF)	
2320 × 900(950) x 35 × 130(80) 2440 × 800(950) x 40 × 80(60)			Linear ($\psi = 1.0$) Distributed load (applied at the top face -TF, the centroid - G, the torsion center - D and the bottom face - BF) Point load (applied at the top face -TF, the centroid - G, the torsion center - D and the bottom face - BF)	

* Doubly symmetric cross-sections.
* * Only applicable to mono-symmetric cross-sections / Not applicable to cases where $\psi = -1.0$.
* ** Only applicable to mono-symmetric cross-sections.

Table 10
Parameters range covered by the parametric study for prismatic beams.

h/b_{min}	b_2/b_1	t_2/t_1	$z_G{}^*/(h/2)$	$W_{y,el,min}/W_{y,el,max}$	Class
1.26 to 3.33	0.84 to 1.75	1.00 to 2.00	0.58 to 1.00	0.41 to 1.00	1 and 2

corresponding deformed shape of LBA and GMNIA for uniform mono-symmetric members subjected to linear bending moments.

Fig. 25 compares the typical deformed shape of LBA and GMNIA for mono-symmetric tapered members subjected to distributed load.

Additional comparisons are available in Annex A. In summary, the GMNIA deformed shape are equivalent to the modal displacements and rotations (and their derivatives) obtained through the LBA analysis.

5.3. Prismatic mono-symmetric cross section

Firstly, for the analysed mono-symmetric beams, it is interesting to note that the numerically calculated elastic critical moments (M_{cr}) are very similar to those obtained using the analytical 3-factor formula for the elastic critical moment [20] as shown in Table 11.

Fig. 26 presents the scatter plot of r_t x r_e for the different loading types for the prismatic mono- and doubly symmetric cross sections subsets, where r_e is the ratio between the numerical lateral-torsional buckling resistance and the plastic bending moment resistance of the cross section, and r_t is the ratio between the analytical buckling resistance (AISC, EC3-General Case or General Formulation) and the cross-sectional plastic bending moment resistance. In general, AISC exhibits a large scatter and unsafe results, while GC and GF lead to safe-sided values. However, GC rules are too conservative for all cases studied, while GF yields more accurate estimates of the lateral-torsional buckling resistance.

The statistical evaluation of AISC, GC and GF (see also Table A.1 to A.3) is carried out based on the ratio (r_N) between the numerical lateral-torsional buckling resistance and the analytical lateral-torsional buckling resistance. Globally, the followings values were obtained (see Table 12): an average $r_N = 1.42$ and a c.o.v of 8.33% for GC, an average $r_N = 1.16$ and a c.o.v of 7.61% for GF and an average $r_N = 0.90$ and a c.o.v of 7.34% for AISC.

Comparing GC and GF, the poor performance of GC is a direct result of the lack of mechanical consistency of the derivation of this method [51]. In contrast, GF adopts the generalized imperfection factors of the mechanically consistent method developed by Taras and Greiner [5] for prismatic double symmetric cross-section beams and leads to similar results as this new method for doubly symmetric cross sections.

Comparison of the results for double- and mono-symmetric cross-sections shows that the results are approximately 2% to 3% worse for mono-symmetric beams for GF, while for GC this difference increases to 4% to 6% (see Tables A.1 to A.3). GC only takes into account the influence of mono-symmetry in the elastic critical bending moment M_{cr} (Eq. (13)), while GF considers this effect both in the M_{cr} determination and in the computation of the imperfection factor (see Eqs. (38) and (40)).

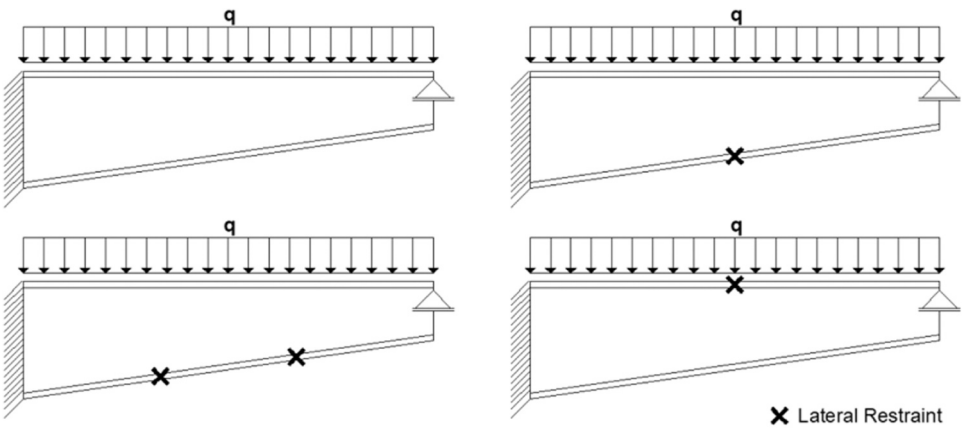

Fig. 20. Cases for tapered members with mono-symmetric I-sections subjected to distributed load.

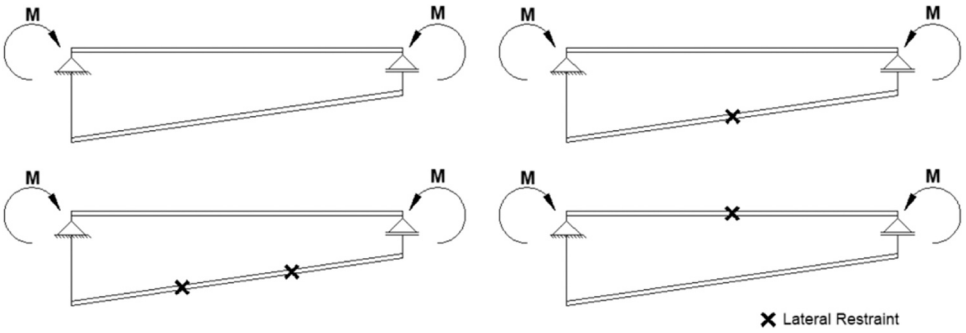

Fig. 21. Cases for tapered members with mono-symmetric I-sections subjected constant bending moment.

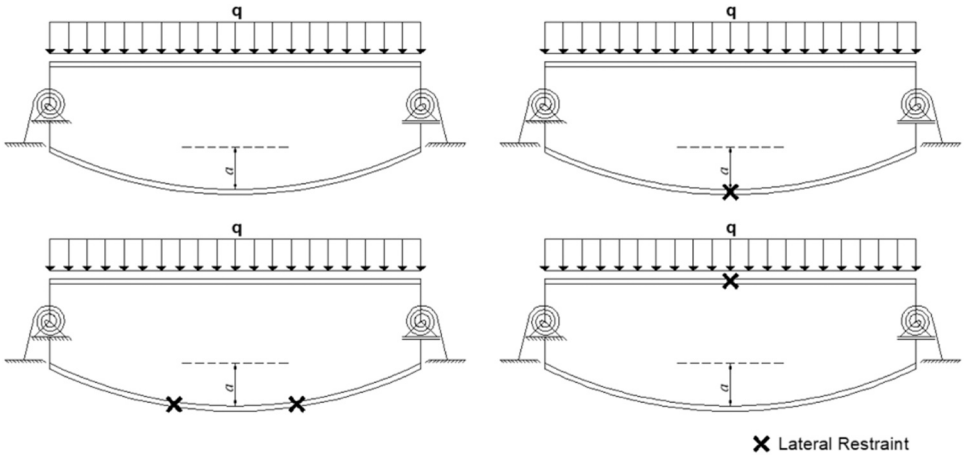

Fig. 22. Cases for parabolic members with mono-symmetric I-section subjected to distributed load.

5.4. *Non-prismatic and tapered mono-symmetric cross-sections*

Fig. 27 show the scatter plot r_t x r_e for the mono-symmetric non-prismatic and tapered beams and Table 13 and Table 14 exhibit the comparison between the numerical lateral-torsional buckling resistance and the corresponding analytical results according to the AISC Guide [42], the General Method (GM), the method proposed by Marques et al. [40] and the proposed extension of the General Formulation (GF), in terms of r_N ratio, for tapered and non-prismatic beams, respectively.

For the tapered beams (see Table 13), AISC and GM show poor results with high scatter that are unacceptably conservative, with an average $r_N = 2.14$ and a c.o.v of 29.85%, and an average $r_N = 1.97$ and a c.o.v of 16.73%, respectively, with AISC being insecure for a few slender beams. AISC and GM methods are time-consuming procedures, where the critical location is obtained through an iterative operation. Furthermore, the definition of the imperfection factors for GM is not clearly defined and may lead to inaccurate results. In contrast, the results of Marques et al. [40] proposal and GF are considerably closer to the numerical values, leading to an average $r_N = 1.20$ and a c.o.v of 11.83%, and an average $r_N = 1.15$ and a c.o.v of 7.52%, respectively, with GF exhibiting a similar performance when compared to the prismatic cases. The design approach of Marques et al. [40] proposal and GF present much higher accuracy than the methods proposed by AISC and GM, because: (i) they use generalized imperfection factors based on mechanically consistent

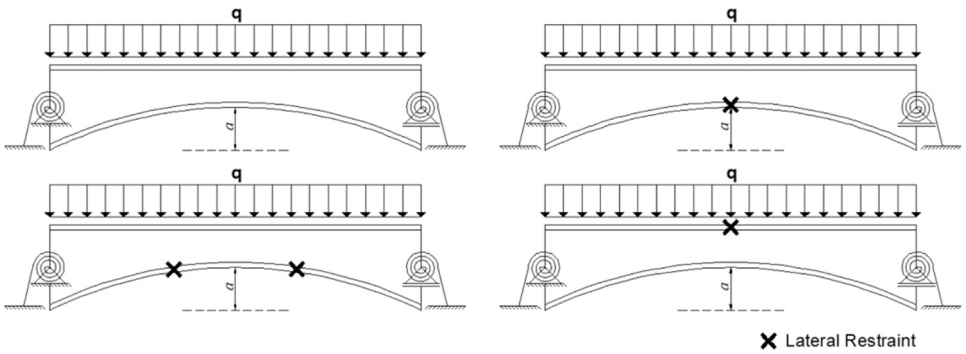

Fig. 23. Cases for anti-parabolic members with mono-symmetric I-section subjected to distributed load.

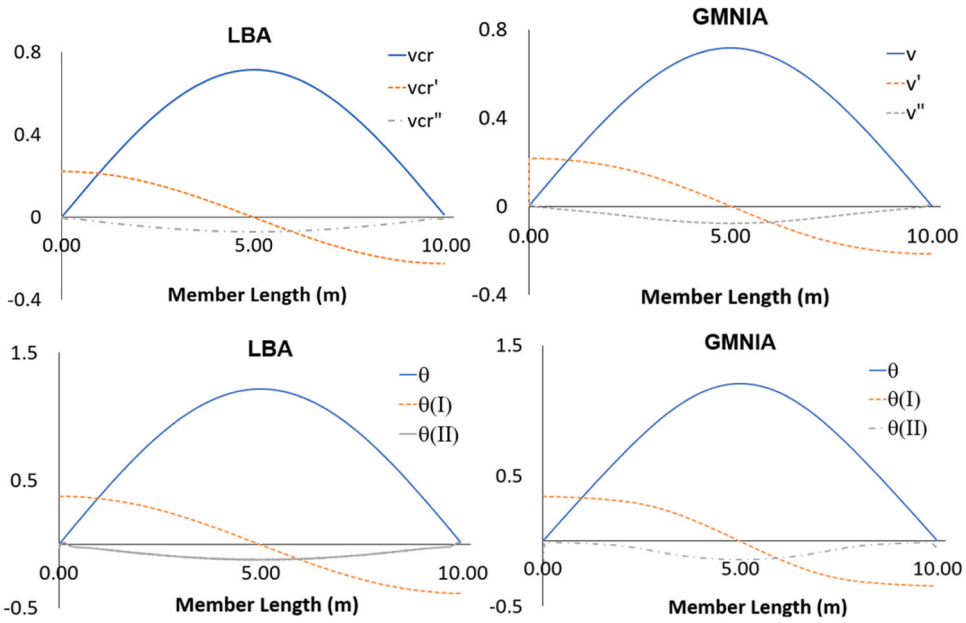

Fig. 24. Mode shape for uniform mono-symmetric beams subjected to linear bending moment ($\psi = 1.0$) - $\bar{\lambda}_z = 2.40$.

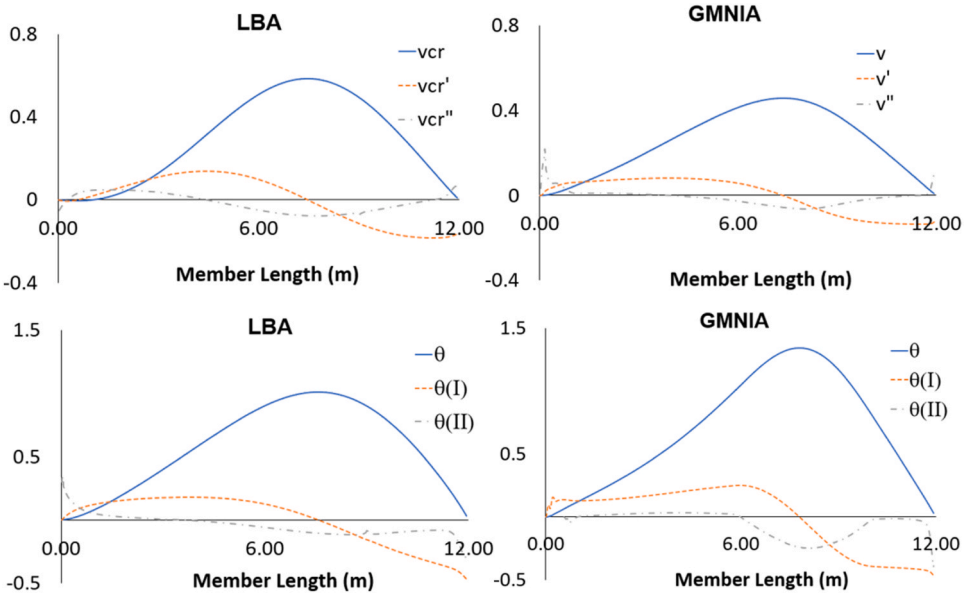

Fig. 25. Mode shape for tapered mono-symmetric beams subjected to distributed load (without restraints along the member) - $\bar{\lambda}_z = 1.30$.

Table 11
Comparison between numerical and analytical [20] values for the elastic critical bending moment for lateral-torsional buckling.

Subset	n	$M_{cr,num}/M_{cr,anal}$	
		Average	COV (%)
All	1296	0.97	6.91
Linear Bending Moment	408	0.96	6.71
Distributed Load	444	0.97	8.22
Point Load	444	0.99	5.07

derivations; and (ii) take into account the effect of the taper. For the cases without intermediate bracings, the method proposed by Marques et al. [40] leads to better results because the generalized imperfection factors and the second-order critical location were specifically calibrated for web-tapered beams, by using an extensive numerical program. However, the method is not applicable to partial lateral bracings (bracing to the tension flange), as shown in Table 13, leading to worse results for these cases.

For the non-prismatic beams, only GM and GF are applicable (see Table 14). GM exhibits unsafe results for the parabolic beams and reasonable results for the anti-parabolic ones, leading to an average $r_N = 0.92$ and a c.o.v of 28.96%, and an average $r_N = 1.30$ and a c.o.v of 8.92%, respectively for both cases. AISC prescriptions do not cover non-prismatic beams. GF gives accurate results (an average $r_N = 1.23$ and a c.o.v of 7.37%, respectively, for the parabolic beams; and an average $r_N = 1.25$ and a c.o.v of 7.48%, respectively, for the anti-parabolic beams).

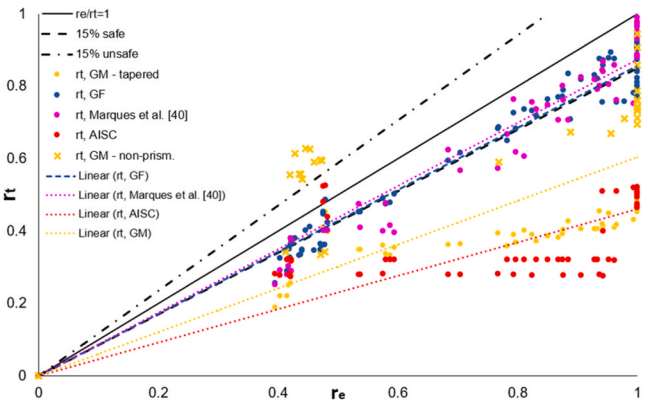

Fig. 27. Scatter plot for the tapered and non-prismatic members.

6. Worked example

The following example aims to demonstrate the step-by-step the application of the General Formulation to mono-symmetric beams. Consider the beam shown in Fig. 28 in steel grade S235. The depth of the beam exhibits a parabolic variation with a mono-symmetric cross-section, subjected to a distributed load (135 kN/m) applied at top face of the cross-section. The cross-section at the member ends is 500 × 200 (150) x 12 × 50(30), with maximum section depth at mid-span equal to 800 mm. The member ends exhibit simply supported conditions boundary conditions except for the in-plane rotation (rotation about the

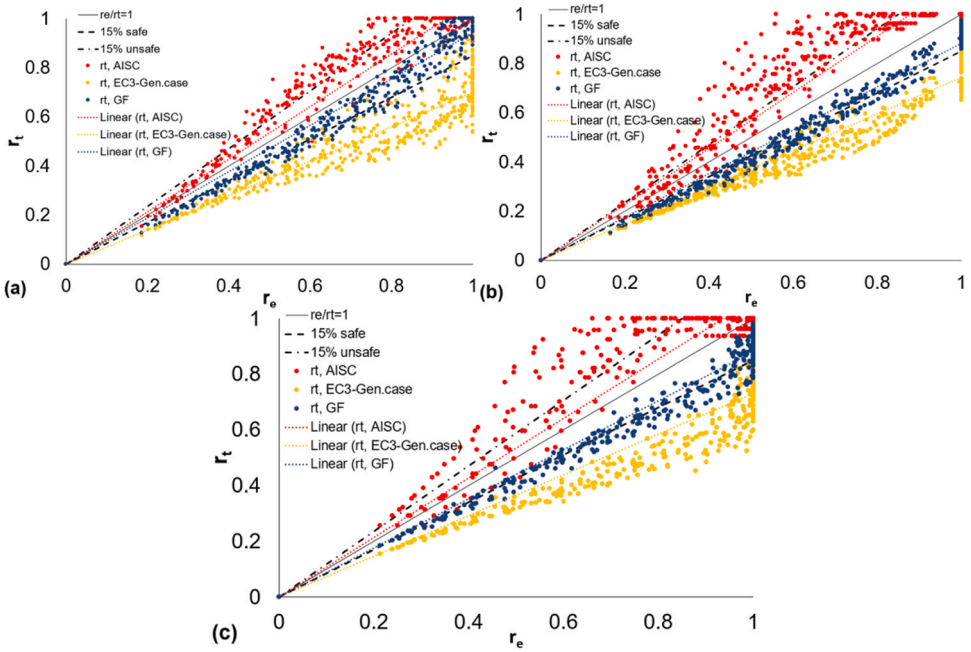

Fig. 26. Scatter plot: (a) linear bending moment, (b) distributed load, (c) point load.

Table 12
Statistical parameters for prismatic members.

Subset	n	$r_{N,AISC}$				$r_{N,GC}$				$r_{N,GF}$			
		Average	Cov (%)	Min	Max	Average	Cov (%)	Min	Max	Average	Cov (%)	Min	Max
All	1296	**0.90**	7.34	0.78	1.08	**1.42**	8.33	1.18	1.65	**1.16**	7.61	1.03	1.31
Linear bending moment	408	**0.93**	7.34	0.81	1.08	**1.41**	8.33	1.20	1.58	**1.13**	7.61	1.03	1.31
Distributed load	444	**0.87**	9.23	0.78	1.00	**1.42**	8.55	1.20	1.59	**1.19**	6.41	1.06	1.30
Concentrated load	444	**0.90**	7.89	0.82	1.01	**1.44**	10.3	1.18	1.65	**1.18**	5.83	1.05	1.26

Table 13
Statistical parameters for the tapered beams.

Subset	n	$r_{N,AISC}$		$r_{N,GM}$		$r_{N,Marques\ et\ al.[40]}$		$r_{N,GF}$	
		Average	Cov (%)	Average	Cov (%)	Average	Cov (%)	Average	Cov (%)
All	56	**2.14**	**29.85**	**1.97**	**16.73**	**1.20**	**11.83**	**1.15**	**7.52**
Distributed load	44	2.39	20.08	2.09	10.13	1.17	10.14	1.15	4.60
Liner bending moment	12	1.25	17.66	1.53	21.28	1.31	12.52	1.19	13.36
No Restraints	14	2.01	27.95	1.98	16.06	1.17	13.65	1.21	10.89
1 restraint at flange in tension	14	2.08	29.49	1.97	17.03	1.24	8.72	1.17	4.77
2 restraints at flange in tension	14	2.12	31.79	1.86	17.66	1.28	11.77	1.12	6.17
1 restraint at flange in compression	14	2.36	30.22	2.06	16.59	1.09	4.80	1.12	2.21
Mono-symmetric cross-sections	40	2.04	28.39	1.99	17.92	1.18	10.98	1.15	6.66
Doubly symmetric cross-sections	16	2.40	30.32	1.91	13.04	1.23	13.52	1.17	9.46

Table 14
Statistical parameters for the non-prismatic beams.

Subset	n	$r_{N,GM}$		$r_{N,GF}$	
		Average	Cov (%)	Average	Cov (%)
Parabolic member	16	0.92	28.96	1.23	7.37
Anti-parabolic member	16	1.30	8.92	1.25	7.48

Note: AISC prescriptions do not cover non-prismatic beams.

y-axis) for the left end, which is restrained by a rotational spring with a stiffness equal to 3.5×10^5 kN.m/rad. Additionally, the tensioned flange is braced at mid-span.

The application of the General Formulation is summarized in the flowchart shown in Fig. 29 for the design of a beam potentially failing by lateral-torsional buckling. Firstly, the user must determine the eigenmode and its corresponding load multiplier, α_{cr}, by using a Linear Buckling Analysis. For the example shown in Fig. 28, the following can be retrieved: $\alpha_{cr} = 1.35183$; Fig. 30 presents separately the mode shape, in terms of lateral displacement (v_{cr}) and twist rotation (θ_{cr}), and their first and second derivatives.

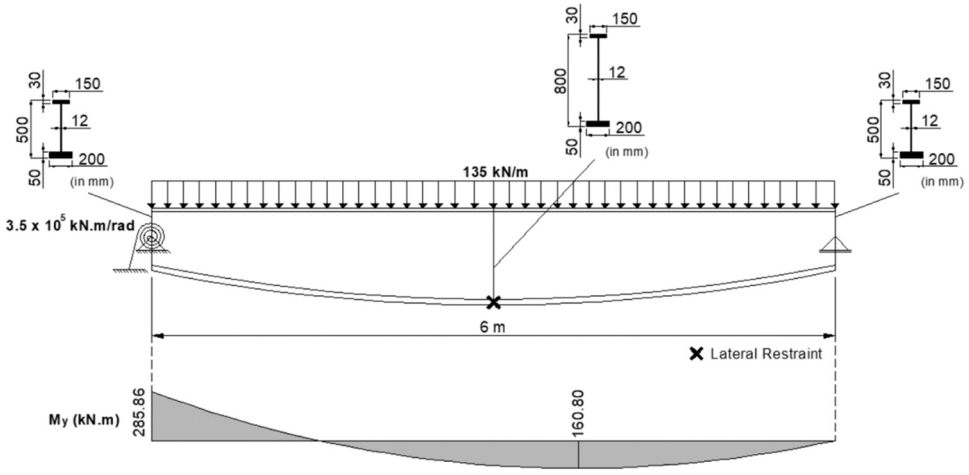

Fig. 28. Worked example: geometry and internal first-order bending moment diagram.

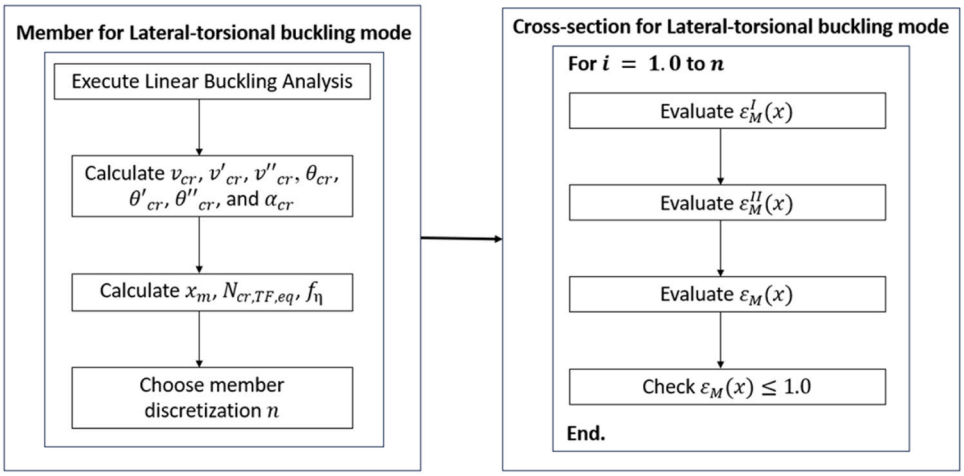

Fig. 29. Application of the method for the lateral-torsional buckling mode.

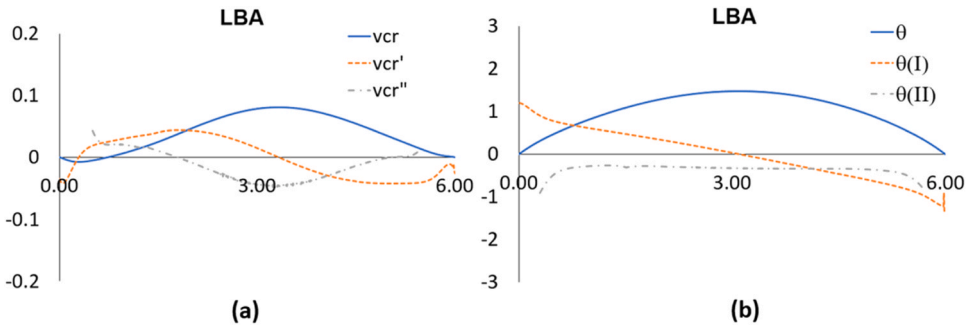

Fig. 30. Mode shape for the parabolic member in terms of $v_{cr}(x)$ and $\theta_{cr}(x)$, and their derivatives.

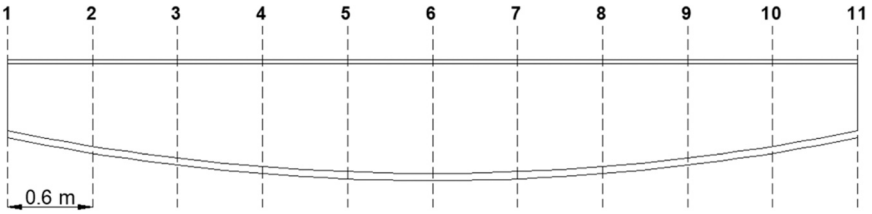

Fig. 31. Member discretization.

Table 15
Geometric properties and internal first order bending moment.

n	x (m)	A (cm^2)	W_y (cm^3)	W_z (cm^3)	I_z (cm^4)	C_w (cm^6)	W_w (cm^4)	$M_{y,Ed}$ $(kN.m)$
1	0	195.40	3265.64	683.87	4183.13	1,424,738.15	4971.84	-285.86
2	0.6	208.39	4354.23	687.77	4184.69	2,174,179.63	6188.10	-154.50
3	1.2	218.50	5253.25	690.80	4185.90	2,866,576.03	7134.94	-45.81
4	1.8	225.68	5917.93	692.95	4186.77	3,416,639.08	7807.84	40.00
5	2.4	229.97	6325.02	694.24	4187.28	3,768,053.38	8209.63	102.89
6	3.0	231.40	6462.49	694.67	4187.45	3,889,077.31	8343.64	142.93
x_m	**3.27**	**231.11**	**6434.84**	**694.58**	**4187.42**	**3,864,640.42**	**8316.75**	**153.44**
7	3.6	229.97	6325.02	694.24	4187.28	3,768,053.38	8209.63	160.08
8	4.2	225.68	5917.93	692.95	4186.77	3,416,639.08	7807.84	154.37
9	4.8	218.50	5253.25	690.80	4185.90	2,866,576.03	7134.94	125.78
10	5.4	208.39	4354.23	687.77	4184.69	2,174,179.63	6188.10	74.32
11	6.0	195.40	3265.64	683.87	4183.13	1,424,738.15	4971.84	0

Table 16
Mode shape and its derivatives for lateral-torsional buckling, considering each cross-section discretized along the member.

n	x (m)	h (mm)	h' $(-)$	v_{cr} $(-)$	v''_{cr} (m^{-2})	θ_{cr} $(-)$	θ'_{cr} (m^{-2})	θ''_{cr} (m^{-2})	$\delta^{fl}(x)$ $(-)$
1	0	500	0	0	0	0	0	0	0
2	0.6	608.25	0.1607	-0.0032	0.0268	0.5554	0.7287	-0.3721	0.2570
3	1.2	692.49	0.1204	0.0140	0.0166	0.9366	0.5527	-0.2569	0.5157
4	1.8	752.34	0.0796	0.0379	0.0009	1.2201	0.3917	-0.2734	0.7498
5	2.4	788.08	0.0399	0.0629	-0.0251	1.4038	0.2195	-0.3011	0.9220
6	3.0	800	0.0002	0.0788	-0.0435	1.4793	0.0320	-0.3229	0.9982
x_m	3.27	797.61	-0.0176	0.0812	**-0.0484**	1.4760	-0.0553	-0.3190	0.9956
7	3.6	788.08	-0.0395	0.0795	-0.0422	1.4392	-0.1647	-0.3348	0.9603
8	4.2	752.34	-0.0792	0.0653	-0.0253	1.2799	-0.3646	-0.3330	0.8121
9	4.8	692.49	-0.1200	0.0422	-0.0043	1.0011	-0.5629	-0.3432	0.5785
10	5.4	608.25	-0.1603	0.0169	0.0062	0.5967	-0.7921	-0.4559	0.2964
11	6.0	500	0	0	0	0	0	0	0

Secondly, it is necessary to calculate the cross-section that corresponds to the critical location, x_m. This is taken as the location where v''_{cr} is maximum. This position occurs in this case at 3.27 m from the left end of the beam. Hence, using Eq. (40), the equivalent elastic critical force is:

$$N_{cr,TF,eq} = \frac{EI_z(x_m)|v''_{cr}(x_m)|}{|v_{cr}(x_m) + z_0\theta_{cr}(x_m)|} = \frac{21000\text{x}10^4\text{x}4187.42\text{x}10^{-8}\text{x}|-0.0484|}{|0.0812 + 0.13749\text{x}1.4760|} = 1497.19kN \tag{42}$$

and, using Eq. (35) the factor f_η becomes:

$$f_\eta = \frac{N_{cr,TF}}{EI_z(x_m)\left[v''_{cr}(x_m) + \frac{W_z(x_m)}{W_w(x_m)}\frac{C_w(x_m)}{I_z(x_m)}\left(\theta''_{cr}(x_m) + \frac{W_w(x_m)}{W_z(x_m)}\frac{I_z(x_m)}{C_w(x_m)}\theta'_{cr}(x_m)h'\right)\right]} = 0.5749 \tag{43}$$

Following the flowchart shown in Fig. 29, the utilization ratio is verified at multiple locations along the member. Thus, the member was

Table 17
Lateral-torsional buckling verification.

n	x (m)	$\bar{\lambda}$	α_{LT}	$M_{y,Ed}$ $(kN.m)$	$\varepsilon_M^I(x)$	$\varepsilon_M^{II}(x)$	$\varepsilon_M(x)$
1	0	1.70	0.51	-285.86	0.38	0.00	0.38
2	0.6	1.76	0.58	-154.50	0.16	0.17	0.33
3	1.2	1.81	0.64	-45.81	0.04	0.29	0.33
4	1.8	1.84	0.64	40.00	0.03	0.44	0.47
5	2.4	1.86	0.64	102.89	0.07	0.69	0.76
6	3.0	1.86	0.64	142.93	0.10	0.86	0.95
x_m	3.27	1.86	0.64	153.44	0.11	0.86	**0.96**
7	3.6	1.86	0.64	160.08	0.11	0.84	0.95
8	4.2	1.84	0.64	154.37	0.12	0.64	0.75
9	4.8	1.81	0.64	125.78	0.11	0.40	0.51
10	5.4	1.76	0.58	74.32	0.08	0.22	0.30
11	6.0	1.70	0.51	0	0.00	0.00	0.00

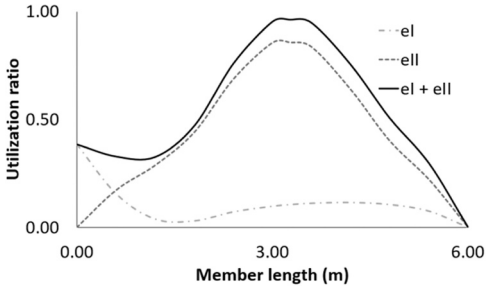

Fig. 32. Utilization ratio for lateral-torsional buckling.

discretized in 10 elements, 0.6 m long, as shown in Fig. 31.

Table 15 summarizes the geometric properties of each cross-section in Fig. 31, as well as the associated internal first order bending moments.

Table 16 summarizes the mode shape for the lateral torsional buckling mode, its derivatives and the general displacement given by Eq. (36), for each discretized cross-section.

Finally, the global utilization ratio ($\varepsilon_M(x)$) for the lateral-torsional buckling mode is calculated using Eq. (37). The utilization ratio due to first order forces is determined for each cross-section by using the bending moment diagram shown in Fig. 28. The generalized imperfection (η) is calculated using Eq. (38):

$$\eta(x) = \alpha_{LT}(x)(\bar{\lambda}(x) - 0.2)f_\eta\left|\delta^{II}(x)\right| = 0.5749\alpha_{LT}(x)(\bar{\lambda}(x) - 0.2)\left|\delta^{II}(x)\right| \tag{44}$$

with the imperfection factor, $\alpha_{LT}(x)$, calculated according to the FprEN 1993–1-1 rules for the lateral-torsional buckling of doubly symmetric I-section welded prismatic members.

Table 17 summarizes the application of Eq. (37), showing a maximum utilization ratio of 0.96, and Fig. 32 illustrates the variation of the utilization ratio along the beam.

7. Conclusions

The General Formulation proposed by Tankova et al. [8] was extended for mono-symmetric beams with variable geometry, and boundary conditions, subject to arbitrary loading. A calibrated advanced FEM numerical model was used to carry out a large parametric study on uniform, tapered, and non-prismatic beams. The parametric study contains mono- and doubly symmetric welded I-sections – steel grade S235, S355, and S460 (Class 1 and 2) - subjected to various bending moment diagrams and boundary condition types. It can be concluded that:

- the AISC approach overestimates the buckling resistance of uniform mono-symmetric beams; however, considering the design value with the application of $\phi = 0.9$, the average ration becomes close to 1.0. For tapered double-symmetric and mono-symmetric beams, AISC yields very conservative results (> 2.0);
- the application of the General Case and the General Method as specified in EC3-1-1 lead to very conservative results for the most cases, the latter exhibiting unsafe results for some cases of the non-prismatic beams subset, as was already concluded in [7];
- the proposal of Marques et al. [40] leads to accurate and secure results for web-tapered beams.
- The extended General Formulation leads to good and consistent results for all cases studied. For tapered beams, the accuracy is like Marques et al. [40]; for non-prismatic beams with complex bracing conditions and supports, the General Formulation maintains the good consistency with the prismatic cases. The results of the General Method are very poor.

The General Formulation is easily incorporated in structural design software because its practical implementation consists of a sequence of cross-sectional checks. Finally, it is noted that in practice many beams will present class 4 cross sections. The authors are currently extending the General Formulation to cope with local buckling.

Declaration of Competing Interest

I declare on behalf of myself and all the authors that there is no conflict of interest.

Data availability

Data will be made available on request.

Acknowledgments

This work was partly financed by:

(i) Coordenação de Aperfeiçoamento de Pessoal de Nível Superior – Brazil (CAPES) – Finance Code 001.
(ii) Conselho Nacional de Desenvolvimento Científico e Tecnológico – Brazil (CNPq) – Process: 439680/2018-2 and 314827/2020-0.
(iii) FCT / MCTES through national funds (PIDDAC) under the R&D Unit Institute for Sustainability and Innovation in Structural Engineering (ISISE), under reference UIDB / 04029/2020, and under the Associate Laboratory Advanced Production and Intelligent Systems ARISE under reference LA/P/0112/2020.

Authors statement

I declare on behalf of myself and all the authors that this paper has not been previously published; it is not currently submitted for review to any other journal and will not be submitted elsewhere during peer review by Engineering Structures.

ANNEX A. – Comparison between LBA and GMNIA Deformed shapes

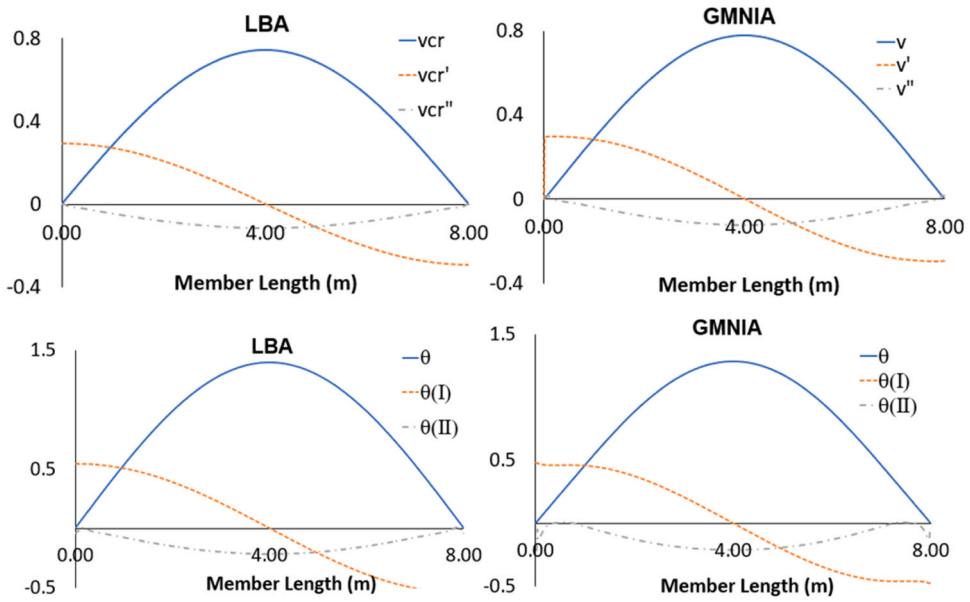

Fig. A1. Mode shape for uniform doubly symmetric beams subjected to linear bending moment ($\psi = 1.0$) - $\overline{\lambda}_z = 1.90$.

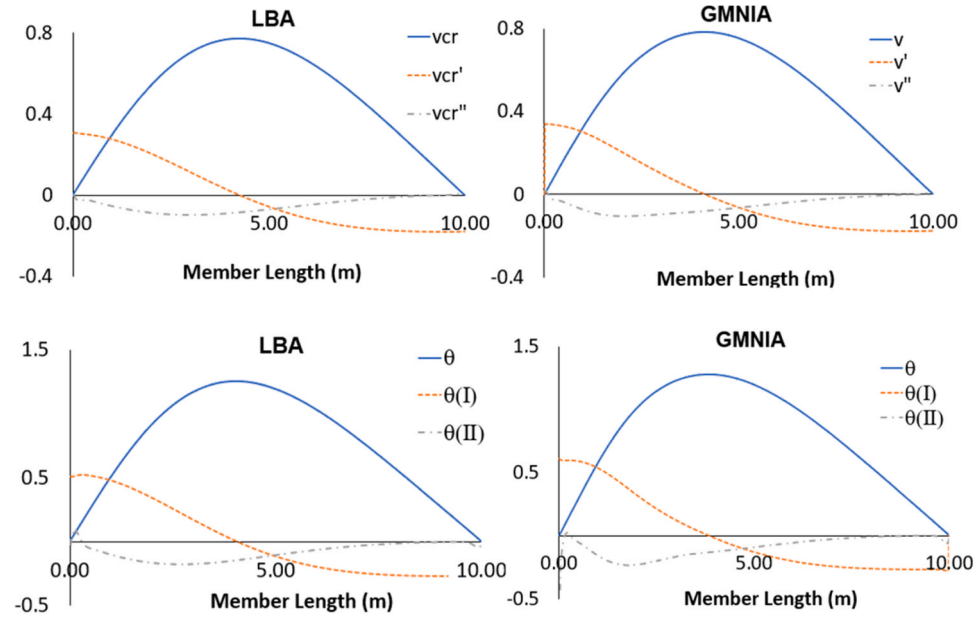

Figure A.2. Mode shape for uniform doubly symmetric beams subjected to linear bending moment ($\psi = 0.0$) - $\overline{\lambda}_z = 2.40$.

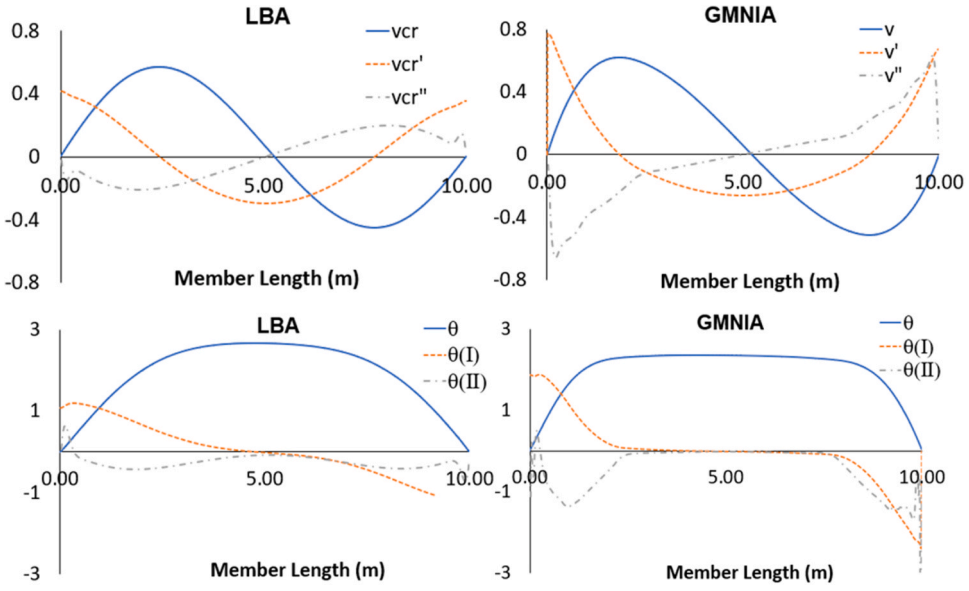

Figure A.3. Mode shape for uniform doubly symmetric beams subjected to linear bending moment ($\psi = -1.0$) - $\bar{\lambda}_z = 2.40$.

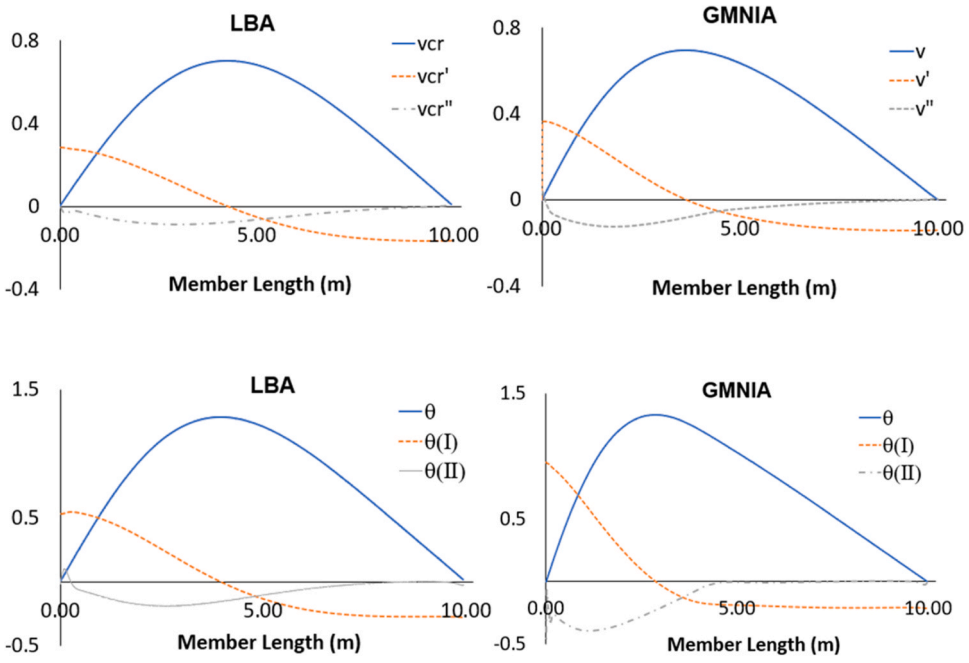

Figure A.4. Mode shape for uniform mono-symmetric beams subjected to linear bending moment ($\psi = 0.0$) - $\bar{\lambda}_z = 2.40$.

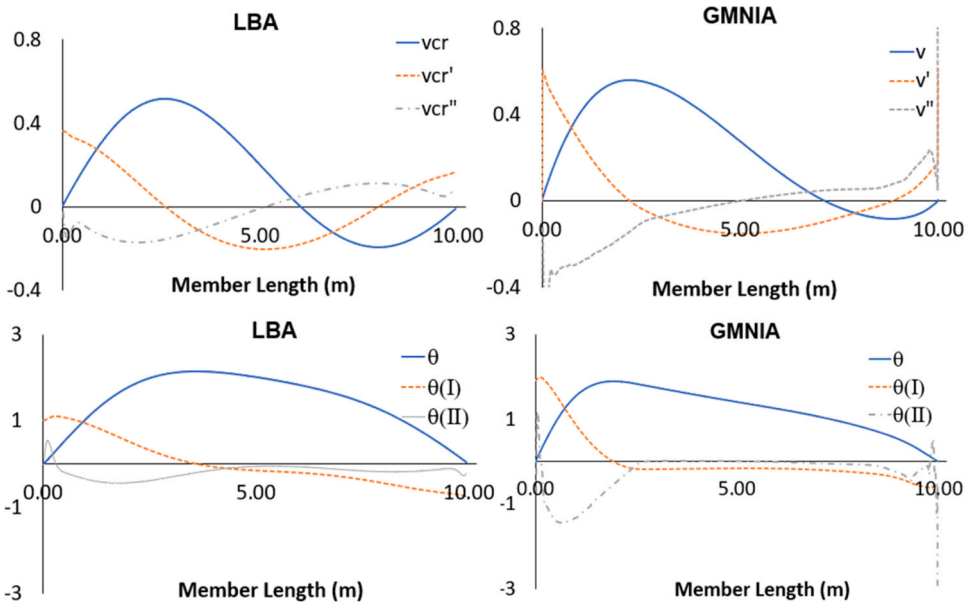

Figure A.5. Mode shape for uniform mono-symmetric beams subjected to linear bending moment ($\psi = -1.0$) - $\overline{\lambda}_z = 2.40$.

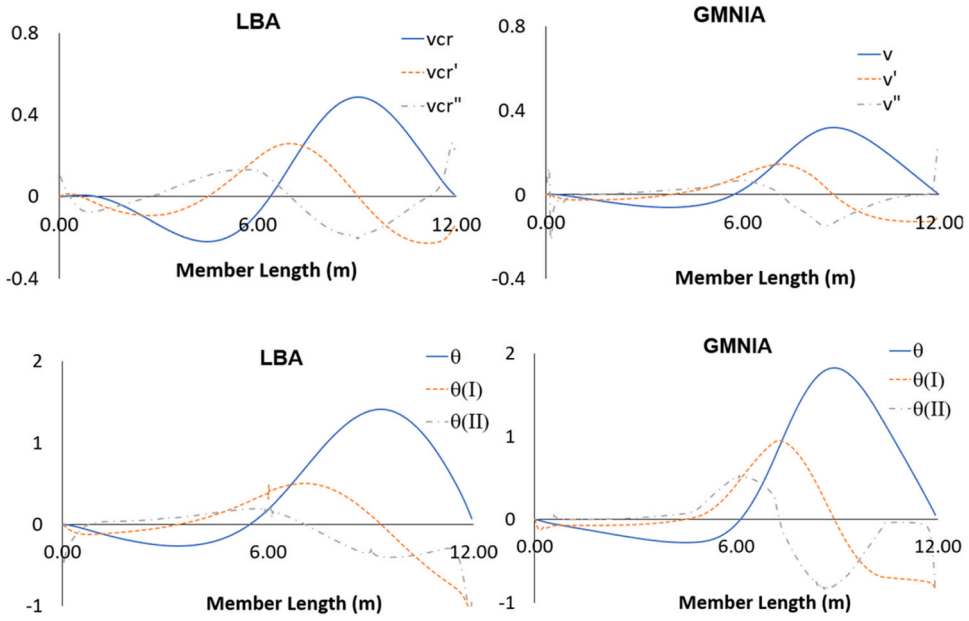

Figure A.6. Mode shape for tapered mono-symmetric beams subjected to distributed load (with lateral restraint at compression flange) - $\overline{\lambda}_z = 1.30$.

ANNEX B. –Detailed statistical assessment for prismatic mono-symmetric cross sections

Table B1
Statistical parameters for linear bending moment distribution.

Linear Bending Moment													
Subset	n	$r_{N,AISC}$				$r_{N,GC}$				$r_{N,GF}$			
		Average	Cov (%)	Min	Max	Average	Cov (%)	Min	Max	Average	Cov (%)	Min	Max
All	408	**0.93**	7.34	0.81	1.08	**1.41**	8.33	1.20	1.58	**1.13**	7.61	1.03	1.31
S235	136	**0.89**	10.09	0.73	1.05	**1.32**	7.93	1.13	1.47	**1.07**	6.30	1.01	1.20
S355	136	**0.93**	7.41	0.82	1.08	**1.43**	8.42	1.21	1.59	**1.14**	8.30	1.04	1.34
S460	136	**0.96**	7.21	0.88	1.11	**1.48**	8.73	1.27	1.67	**1.19**	8.49	1.04	1.39
$\psi = 1.0$	204	**0.90**	8.83	0.81	1.08	**1.39**	8.03	1.20	1.58	**1.17**	6.47	1.03	1.31
$\psi = 0.0$	132	**0.93**	1.08	0.92	0.94	**1.54**	5.55	1.43	1.60	**1.06**	1.92	1.04	1.09

(*continued on next page*)

Table B1 (*continued*)

Linear Bending Moment													
Subset	n	$r_{N,AISC}$				$r_{N,GC}$				$r_{N,GF}$			
		Average	Cov (%)	Min	Max	Average	Cov (%)	Min	Max	Average	Cov (%)	Min	Max
$\psi = -1.0$	72	**0.99**	2.17	0.96	1.02	**1.46**	5.20	1.34	1.52	**1.02**	1.80	1.00	1.05
Stress on Fl. > I_z = Ten., $\psi = 0$; $\psi = 1$	192	**0.89**	8.23	0.81	1.08	**1.43**	8.37	1.20	1.62	**1.14**	7.08	1.06	1.31
Stress on Fl. > I_z = Comp., $\psi = 0$; $\psi = 1$	120	**0.93**	1.36	0.91	0.95	**1.50**	6.05	1.38	1.57	**1.12**	1.07	1.11	1.14
Mono-symmetric cross-section	348	**0.92**	7.81	0.81	1.08	**1.42**	7.88	1.20	1.58	**1.14**	7.45	1.06	1.31
Doubly symmetric cross section	60	**0.94**	6.91	0.90	1.02	**1.38**	11.17	1.21	1.51	**1.12**	9.68	1.03	1.24

Table B2
Statistical parameters for distributed load.

Distributed Load													
Subset	n	$r_{N,AISC}$				$r_{N,GC}$				$r_{N,GF}$			
		Average	Cov (%)	Min	Max	Average	Cov (%)	Min	Max	Average	Cov (%)	Min	Max
All	444	**0.87**	9.23	0.78	1.00	**1.42**	8.55	1.20	1.59	**1.19**	6.41	1.06	1.30
S235	148	**0.84**	11.52	0.70	1.00	**1.34**	9.32	1.13	1.56	**1.13**	5.66	1.04	1.23
S355	148	**0.87**	9.76	0.77	1.00	**1.44**	8.71	1.21	1.60	**1.20**	6.87	1.07	1.32
S460	148	**0.89**	10.08	0.77	1.01	**1.48**	8.43	1.26	1.69	**1.24**	7.35	1.08	1.37
Point load application = TF	120	**0.78**	16.25	0.78	1.00	**1.44**	10.67	1.21	1.75	**1.23**	7.78	1.07	1.35
Point load application = BF	120	**0.94**	8.41	0.85	1.09	**1.41**	8.26	1.19	1.58	**1.17**	5.80	1.06	1.26
Point load application = G	120	**0.88**	8.23	0.80	1.00	**1.41**	8.19	1.20	1.59	**1.18**	6.82	1.06	1.31
Point load application = D	84	**0.87**	7.82	0.80	1.00	**1.30**	25.81	0.59	1.59	**1.18**	6.92	1.06	1.29
Mono-symmetric cross-section	336	**0.86**	9.02	0.78	1.00	**1.43**	8.90	1.20	1.59	**1.20**	6.48	1.06	1.30
Doubly symmetric cross section	108	**0.90**	10.80	0.81	1.00	**1.38**	8.59	1.24	1.47	**1.17**	7.22	1.08	1.25

Table B3
Statistical parameters for point load.

Point Load													
Subset	n	$r_{N,AISC}$				$r_{N,GC}$				$r_{N,GF}$			
		Average	Cov (%)	Min	Max	Average	Cov (%)	Min	Max	Average	Cov (%)	Min	Max
All	444	**0.90**	7.89	0.82	1.01	**1.44**	10.03	1.18	1.65	**1.18**	5.83	1.05	1.26
S235	148	**0.88**	11.43	0.75	1.00	**1.36**	10.93	1.11	1.60	**1.14**	5.43	1.03	1.24
S355	148	**0.91**	8.21	0.83	1.02	**1.45**	10.15	1.19	1.67	**1.18**	6.05	1.05	1.27
S460	148	**0.93**	7.38	0.84	1.01	**1.49**	9.54	1.23	1.67	**1.21**	6.45	1.06	1.33
Point load application = TF	120	**0.80**	17.46	0.64	1.00	**1.44**	10.75	1.19	1.65	**1.19**	6.01	1.04	1.28
Point load application = BF	120	**0.99**	6.29	0.93	1.14	**1.43**	10.49	1.16	1.64	**1.16**	6.19	1.04	1.24
Point load application = G	120	**0.92**	7.15	0.83	1.01	**1.44**	10.24	1.18	1.66	**1.18**	6.23	1.04	1.29
Point load application = D	84	**0.91**	8.05	0.83	1.01	**1.45**	10.18	1.19	1.67	**1.18**	6.28	1.05	1.25
Mono-symmetric cross-section	336	**0.90**	8.07	0.82	1.01	**1.45**	9.86	1.18	1.65	**1.18**	6.24	1.05	1.26
Doubly symmetric cross section	108	**0.91**	9.22	0.84	1.00	**1.39**	11.90	1.20	1.51	**1.16**	5.75	1.09	1.22

References

[1] Martins JP, Correia JN, Ljubinkovic F, Simões da Silva L. Cost optimization of steel I-girder cross-sections using genetic algorithms. Struct 2023;55:379–88.
[2] EN 1993-1-1. Eurocode 3: Design of steel structures - Part 1-1: General rules and rules for buildings. Brussels: Comité Européen de Normalisation (CEN); 2005.
[3] Simões da Silva L, Simões R, Gervásio H. Design of steel structures. 2nd ed. ECCS eurocode design manuals. Wiley and ECCS Press; 2016.
[4] FprEN 1993-1-1. Eurocode 3: Design of steel structures – Part 1-1: General rules and rules for buildings. Brussels: Comité Européen de Normalisation (CEN); 2022.
[5] Taras A, Greiner R. New design curves for lateral-torsional buckling – proposal based on a consistent derivation. J Constr Steel Res 2010;66(5):648–63.
[6] Taras A. Contribution to the development of consistent stability design rules for steel members. PhD Thesis. Austria: Technical University of Graz; 2010.
[7] Simões da Silva L, Marques L, Rebelo C. Numerical validation of the general method in EC3-1-1: lateral, lateral-torsional and bending and axial force interaction of uniform members. J Constr Steel Res 2010;66:575–90.
[8] Tankova T, Simões da Silva L, Marques L. Buckling resistance of non-uniform steel members based on stress utilization: general formulation. J Constr Steel Res 2018; 149:239–56.
[9] Vlassov BZ. Pièces longues en voiles minces, traduit par Smirnoff G.. Paris: Editions Eyrolles; 1962.
[10] Wagner H. Torsion and buckling of open sections. NACA Tech Mem 1936;(807)).
[11] Kitpornchai S, Trahair NS. Buckling Properties of Monosymmetric I-Beams. Proc ASCE J Struct Div 1980;106(5).
[12] Roberts TM, Burt CA. Instability of monossymetric I-beams and cantilevers. Int J Mech Sci 1985;27(5):313–24.
[13] Roberts TM, Azizian ZG. Influence of pre-buckling displacements on the elastic critical loads of thin-walled bars of open cross-section. Int J Mech Sci 1983;25: 93–104.
[14] Roberts TM. Second-order strains and instability of thin-walled bars of open cross-section. Int J Mech Sci 1981;23:297–306.
[15] Wang CM, Kitipornchai S. On stability of monosymmetric cantilevers. Eng Struct 1986;8(3):169–80.
[16] Wang CM, Kitipornchai S, Thevendran V. Buckling of braced monosymmetric cantilevers. Int J Mech Sci 1987;29(5):321–37.
[17] Goodier J.N. Flexural-torsional buckling of bars of open section under bending, eccentric thrust or torsional loads. Bulletin 28: Cornell University Engineering Experimental Station; 1942.
[18] Anderson JM, Trahair NS. Stability of monosymmetric beams and cantilevers. Proc ASCE: J Struct Div 1972;98:269–86.
[19] Clark JW, Hill HN. Lateral Buckling of Beams. Proc ASCE: J Struct Div 1960;68 (ST7).
[20] ENV 1993-1-1. Eurocode 3: Design of steel structures. Part 1-1: General rules and rules for buildings. Brussels: Comité Européen de Normalisation (CEN); 1992.
[21] Andrade A, Camotim D, Providência e Costa P. On the evaluation of elastic critical moments in doubly and singly symetric I-section cantilevers. J Constr Steel Res 2007;63:894–908.
[22] Camotim D, Andrade A, Basaglia C. Some thoughts on a surprising result concerning the lateral-torsional buckling of monosymmetric I-section beams. Thin-Walled Struct 2012;60:216–21.
[23] Galéa Y. LTBeam – Lateral-torsional buckling of Beams. Centre Technique Industrial de la Construction Métallique (CTICM). At: ⟨https://www.cticm.com/⟩ (version 1.0.10) 2010.

[24] Nethercot DA. Inelastic buckling of monosymmetric I-beams. Proc ASCE J Struct Div 1973;99(ST7):1696–701.
[25] Mohri F, Damil N, Potier-Ferry M. Linear and non-linear stability analyses of thin-walled beams wit monosymmetric I sections. Thin-Walled Struct 2010;48:299–315.
[26] Trahair NS. Inelastic buckling design of monosymmetric I-beams. Eng Struct 2012; 34:564–71.
[27] Surla AS, Kang SY, Park JS. Inelastic buckling assessment of monosymmetric I-beams having stepped and non-compact flange sections. J Constr Steel Res 2015; 114:325–37.
[28] Tankova T, Rodrigues F, Leitão C, Martins C, Simões da Silva L. Lateral-torsional buckling of high strength steel beams: experimental resistance. Thin-Walled Struct 2021;164:107913.
[29] Yang B, Kang SB, Xiong G, Nie S, Hu Y, Wang S. Experimental and numerical study on lateral-torsional buckling of singly symmetric Q460GJ steel I-shaped beams. Thin-Walled Struct 2017;113:205–16.
[30] Kang SB, Yang B, Zhang Y, Elchalakani M, Xiong G. Global buckling of laterally unrestrained Q460GJ beams with singly symmetric I-sections. J Constr Steel Res 2018;145:341–51.
[31] Zhao J, Li J, Sun Y. Experimental and numerical study on overall buckling behavior of Q460 high-strength steel continuous beams with welded singly symmetric I-section. Eng Struct 2023;280:115678.
[32] Bradford MA, Cuk PE. Elastic buckling of tapered monosymmetric I-beams. J Struct Eng 1988;114:977–96.
[33] Andrade A, Camotim D. Lateral-torsional buckling of singly symmetric tapered beams: theory and applications. J Eng Mech 2005;131:586–97.
[34] Andrade A, Camotim D, Dinis PB. Lateral-torsional buckling of singly symmetric web-tapered thin-walled I-beams: 1D model vs. shell FEA. Comp Struct 2007;85: 1343–59.
[35] Cockalingam SN, Pandurangan V, Nithyadharan M. Timoshenko beam formulation for in-plane behavior of tapered monosymmetric I-beams: analytical solution and exact stiffness matrix. Thin-Walled Struct 2021;162:107604.
[36] Trahair NS, Ansourian P. In-plane behaviour of mono-symmetric tapered beams. Eng Struct 2016;108:53–8.
[37] Trahair NS. Bending and buckling of tapered steel beam structures. Eng Struct 2014;59:229–37.
[38] Trahair N. Lateral buckling of tapered members. Eng Struct 2017;151:518–26.
[39] Abdelrahman AHA, Lotfy S, Liu SW. Generalized line-element formulations for geometrically nonlinear analysis of nonsymmetric tapered steel members with warping and Wagner effects. Eng Struct 2022;273:115052.
[40] Marques L, Simões da Silva L, Greiner R, Rebelo C, Taras A. Development of a consistent design procedure for lateral-torsional buckling of tapered beams. J Constr Steel Res 2013;89:213–35.
[41] ANSI/AISC360-16. Specification for structural steel buildings. Chicago: American Institute of Steel Construction; 2016.
[42] Kaehler RC, White DW, Kim YD. Frame design using web-tapered members, steel design guide 25. Chicago: Metal Building Manufacturers Association and AISC; 2011.
[43] Chen F, Astuta T. Theory of beam-columns Vol. 2: Space behaviour and design. McGraw-Hill; 1977.
[44] ANSYS 22.0. Release 22.0 documentation for ANSYS: guide to the ANSYS documentation. ANSYS Inc. and ANSYS Europe Ltd.; 2021.
[45] Ferreira Filho JO, Tankova T, Carvalho H, Martins CS, Simões da Silva L. Experimental and numerical flexural buckling resistance of high strength steel columns and beam-columns. Eng Struc 2022;265:114414.
[46] ECCS. Manual on stability of steel structures. Brussels: European Convention for Constructional Steelwork; 1976.
[47] Yun X, Gardner L. Stress-strain curves for hot-rolled steels. J Constr Steel Res 2017; 133:36–46.
[48] prEN 1993-1-14. Eurocode 3: Design of steel structures: Part 1-14: Design assisted by finite element analysis. Brussels: Comité Européen de Normalisation (CEN); 2023.
[49] Snijder HH, van der Aa RP, Hofmeyer H, van Hove BWEM. Lateral torsional buckling design imperfections for use in non-linear FEA. Steel Constr 2018;11: 49–56.
[50] Lebastard M. Stability of welded I-section steel members. PhD Thesis. France: INSA Rennes; 2022.
[51] Tankova T, Simões da Silva L, Rodrigues F. Buckling curve selection for HSS welded I-section member. Thin-Walled Struct 2022;177:109430.